

Chapter 3

Photoluminescence Processes in ZnO Thin Films and Quantum Structures

L. M. Kukreja and P. Misra

Abstract ZnO, a well-known direct and wide bandgap semiconductor is found to show intricate photoluminescence (PL) spectra in thin films and quantum structures such as quantum wells and quantum dots (QDs). In ZnO, thin films grown on sapphire substrates using pulsed laser deposition (PLD) an intense PL in the UV region at about 3.35 eV was observed, which corresponded to near band-edge emission due to the excitonic recombinations. The deep level emission in the visible spectral region of 2–3 eV, which is found to be due to off stoichiometry of the ZnO films, i.e., oxygen vacancies, zinc interstitial, and other structural defects, was almost negligible compared to the near band-edge emission. The strong near band-edge emission in UV spectral region was found to have fine structures consisting of various peaks mainly due to donor and acceptor bound excitons and their phonon replicas, which changed their position and intensity with temperature. In ZnO/Mg_xZn_{1-x}O multi-quantum wells (MQWs) with well layer thickness in the range of ~4 to 1 nm on (0001) sapphire substrates also grown using PLD under the optimized conditions, we observed size-dependent blue shift in ZnO bandgap due to the quantum confinement effect. The PL spectra of these ZnO MQWs recorded at 10 K showed that line width of the PL peaks increased with decreasing well layer thickness, which was attributed to fluctuations in the well layer thickness. The temperature-dependent PL peak positions for the MQWs were found to shift gradually toward red end of the spectrum with increase in temperature up to 300 K due to the temperature-dependent thermal expansion/dilation of the lattice and carrier-phonon scattering. This dependence was found to be consistent with the well-known Varshni's empirical relation. Ensembles of alumina capped ZnO quantum dots (ZQDs) also grown using pulsed laser deposition with mean radii comparable to and smaller than the pertinent excitonic Bohr radius (~2.34 nm), called ultra-small QDs showed size-dependent optical absorption edges. These absorption spectra were found to be consistent with the strong confinement model,

L. M. Kukreja (✉) · P. Misra
Laser Materials Processing Division, Raja Ramanna Centre for Advanced Technology,
P.O. CAT, Indore 452 013, India
e-mail: kukreja@rrcat.gov.in

in which the confinement energy and Coulombic interaction energy of the localized electron-hole pairs are taken to be significantly higher than their correlation energy and the optical transitions are perceived to be non-excitonic in nature. In PL spectra of such ZQDs of mean radius of ~ 2.3 nm at temperatures of ~ 6 K and above the primary recombinations were found to be due to the surface bound and Al donor bound electron-hole pairs. The near band-edge recombination peaks of the PL spectra appeared at the sample temperature of ~ 70 K and beyond. These peaks were found to be ~ 166 meV Stoke and/or thermally red shifted with respect to the experimentally observed absorption edge. Almost all the PL spectra of the ZQDs at different temperatures showed the LO and 2 LO phonon replicas of the primary transitions, which suggests strong coupling between the recombining charge carriers and the LO phonons. The temperature-dependent spectral positions of the PL peaks for the ZQDs also followed the above stated Varshni's relation with fitting parameters close to that of the bulk ZnO. The intensity of the PL peaks was found to follow the normal mechanism of thermal quenching which could be fitted with the Arrhenius type of equation having activation energy of ~ 10 meV. Temperature dependence of FWHM of the PL peaks when fitted with the Hellmann and O'Neill models did not result in a close match. Although one could estimate a value of the carrier-LO phonon coupling coefficient of ~ 980 meV from this fit, but this was found to be much higher than that reported earlier for the ZQDs. These studies are expected to provide deeper insight into the basic optical processes in ZnO thin films, quantum wells, and QDs.

3.1 Introduction

Currently, wide bandgap semiconductor ZnO and its variants are of substantial interest for their applications in UV-blue photonic and transparent electronic devices [1–7]. ZnO is a well-known II–VI oxide semiconductor, which is pyroelectric, piezoelectric, piezooptic, luminescent, and good thermal conductor. It has a direct and wide bandgap of ~ 3.34 eV at room temperature (RT) and hence transparent in the visible spectral region. It has a large excitonic binding energy of ~ 60 meV [8] which is more than two times larger than the room temperature thermal excitation energy of ~ 26 meV. Therefore excitonic transitions can be observed in ZnO at temperatures much larger than room temperature. ZnO naturally crystallizes in rugged hexagonal wurtzite structure and is nominally *n*-type. The high cohesive energy of ZnO, which is ~ 1.89 eV makes it highly stable and perhaps one of the most radiation hard materials among the direct bandgap semiconductors' family [9, 10], which ensures a long life and a high degradation threshold of ZnO-based devices. The high melting point of ZnO (~ 1975 °C) allows one to explore variety of heat treatments required for alloying purpose and device formation. Moreover, ZnO is free from the oxidation problem, which can

severely affect the device performance in the case of oxidation prone semiconductors.

Conventionally, ZnO has been used for transparent conducting electrodes, surface acoustic wave devices, varistors, oxygen sensors, green phosphor for display devices, UV screens, and cosmetics etc. [11, 12]. The current spurt in ZnO research is motivated to develop the futuristic robust and environment friendly technology for the photonic devices operating in short wavelength regimes, i.e., UV-blue spectral region such as light-emitting diode (LED), diode laser, solar blind UV photo-detectors, transparent electronics, and magneto optical devices. These devices could be based on ZnO epitaxial thin films and/or quantum structures of different dimensionality [1, 2, 5, 13]. The observation of stimulated emission and laser oscillations at RT at a low threshold of optical pumping in high-quality ZnO thin films grown on sapphire substrates indicated that the exciton related-transitions at room temperature could be utilized for optoelectronic and nonlinear optical devices [14]. The size-dependent quantum confinement effects in ZnO quantum structures also result in large oscillator strength, enhanced excitonic binding energy, tunability of operating wavelength, and low threshold of lasing [15, 16].

The excitonic transitions are very sensitive to the crystalline quality of the material and therefore growth of thin films and nanostructures with high crystalline quality and stoichiometry are crucial to observe an efficient and stable light emission in the UV-blue spectral region due to recombination of free excitons [17]. Since optoelectronic devices such as light-emitting diodes and laser diodes are based on the fundamental processes of emission, it is imperative to study the optical emission characteristics of high-quality ZnO thin films and low dimensional structures in detail.

In the following sections, we discuss the basics of various photoluminescence (PL) processes occurring in ZnO in general such as recombination of free and bound excitons, LO phonon-assisted recombination of excitons, deep level transitions and effect of quantum confinement on the PL processes in ZnO. The details about the experimental setup used for the PL spectroscopy of ZnO will be presented. This will be followed by a detailed discussion on the results of our studies on the PL spectroscopy of ZnO thin films, quantum well, and dots. Various existing theoretical models have been applied to understand the experimental observations and those will also be presented and discussed in this chapter.

3.2 Fundamentals of Photoluminescence Processes in ZnO

In direct bandgap semiconductors like ZnO, the emission of photon results due to a process reverse of the absorption [18]. The photons of the incoming light beam are absorbed in the semiconductor material to produce free electrons and holes in the conduction and valence band, respectively, which result in the formation of free excitons. Under equilibrium conditions, excitons make transition to an empty

ground state and emit electromagnetic radiation of photon energy equal to the bandgap. This process is commonly known as PL. The energy distribution of photon (PL) is measured to determine properties of the material, including defect species, defect concentrations, possible stimulated emission [18], etc. In intrinsic ZnO, the near band-edge PL process is dominated by excitonic recombination and their longitudinal optical (LO) phonon-assisted transitions. To understand the PL processes in ZnO, it is imperative to discuss the physics of excitons in ZnO and their recombination dynamics. In the following sections, we will give a brief introduction to the ZnO band structure, free and bound excitons and their phonon replicas, deep level transitions, and effect of quantum confinement on the PL processes in ZnO thin films.

3.2.1 Band Structure and Excitons

Since ZnO is a direct bandgap (~ 3.3 eV at room temperature) semiconductor, the maxima of valence band and the minima of conduction band in ZnO lie at the same point in the Brillouin zone, namely at $K = 0$, i.e., at the Γ -point. The ZnO conduction band (CB) is mainly constructed from the empty 4s states of Zn^{+2} ions and has Γ_7 symmetry. The valence band (VB) in ZnO originates from the occupied 2p orbitals of O^{-2} ions and is split into three doubly degenerated bands due to the influence of crystal-field and spin-orbit interactions [3, 14, 15]. A schematic of the ZnO band structure is shown in Fig. 3.1a, b. The three valence bands are labeled from top to bottom suffixes A, B, and C, respectively. The top valence band A has Γ_7 symmetry while the two lower bands B and C have Γ_9 and Γ_7 symmetries, respectively [3, 14]. The splitting of the A and B valence bands and B and C valence bands are of the order of ~ 6 and ~ 38 meV, respectively [2, 8, 19, 20]. The transitions from the two upper valence bands VB_A (Γ_7) and VB_B (Γ_9) to the conduction band CB (Γ_7) are allowed only for the light polarized in the orientation $E \perp c$ and the transitions from the CB (Γ_7) to VB_C (Γ_7) is allowed only for the light polarized in the orientation $E // c$ [2, 20]. These transitions are explicitly shown in Fig. 3.1a. The effective electron mass m_e^* has value $\sim (0.28 \pm 0.02) m_0$ and is almost isotropic [21]. The effective hole masses for the A and B valence bands are also isotropic and have similar value of $m_h^*(\perp, //)_{A,B} = 0.59 m_0$, while for C valence bands the effective hole mass has typical value of $m_h^* // c = 0.31 m_0$ and $m_h^* \perp c = 0.55 m_0$ [20].

Generally in high-quality ZnO crystals and epitaxial thin films and at low excitation density, the electrons and holes generated by the absorption of a photon of suitable energy can pair due to Coulombic attraction to form an exciton [18, 21]. This electron-hole system coupled through Coulombic interaction is known as free exciton. The energy of the free excitons can be calculated by introducing Coulombic interaction term in the Schrödinger equation and is expressed as [18, 21]:

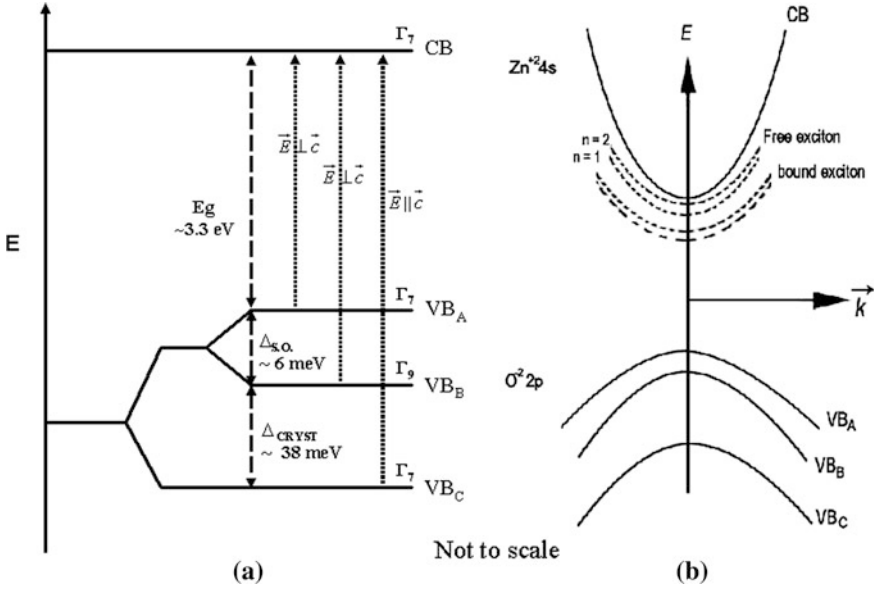


Fig. 3.1 Schematic of ZnO band structure **a** energy level diagram showing the allowed upward transitions with *dotted lines* and **b** E - K diagram showing free and bound exciton energy levels below conduction band with *dotted and dashed lines* respectively

$$E_{\text{ex}} = \frac{m_r^* q^4}{2h^2 \epsilon^2} \cdot \frac{1}{n^2} = -E_B \cdot \frac{1}{n^2} \tag{3.1}$$

where n is an integer and represents different energy states of the excitons and m_r^* is the reduced mass of exciton, which can be given by the following relation:

$$\frac{1}{m_r^*} = \frac{1}{m_e^*} + \frac{1}{m_h^*} \tag{3.2}$$

where m_e^* and m_h^* are the effective masses of electron and hole, respectively. The reduced mass of free exciton is always lower than that of the effective mass of free electron or free hole.

The exciton energy levels E_{ex} are defined with respect to conduction band-edge and the bottom of the conduction band is treated as continuum ($n = \infty$). A schematic representation of the free exciton energy levels corresponding to different n and with respect to the E - K diagram is shown in Fig. 3.1b by dotted lines. The separation $E_{\text{ex}}(n = \infty) - E_{\text{ex}}(n = 1)$ is equal to the binding energy (E_B) of free exciton [18]. The binding energy of exciton is the measure of its stability against temperature. At sufficiently high temperatures, with corresponding thermal energy larger than that of the free exciton binding energy, the excitons dissociate into free electrons and holes.

The free exciton as a pair of opposite charges is free to move in the crystal and hence posses kinetic energy. The kinetic energy of the free excitons can be represented as [18, 21]:

$$E_{ke} = \frac{\hbar^2 K^2}{2(m_e^* + m_h^*)} \quad (3.3)$$

where K is the exciton wavevector associated with the motion of centre of gravity of excitons. The total energy of exciton including the kinetic energy can be represented as:

$$E_{ex} = E_g - \frac{E_B}{n^2} + E_{ke} \quad (3.4)$$

where E_g is the bandgap of the material. Addition of kinetic energy to the exciton energy results in the broadening of excitonic energy levels [18, 21].

The formation of excitons usually appears as narrow peak in the absorption of the direct bandgap semiconductors at photon energies [18, 21]:

$$h\nu = E_g - E_B(1/n^2) \quad (3.5)$$

where E_B is the binding energy of free excitons. Similarly the excitons generated during the optical absorption process recombine, emitting a narrow spectral line at a photon energy given by Eq. 3.5. Since excitons can have series of excited states, hence free excitonic absorption or emission spectra consist of series of narrow lines or peaks occurring at values given by Eq. 3.5. However, the intensity of the higher order peaks decreases rapidly with increasing n [19]. The excitonic absorption and luminescence in semiconductors are governed by the fact that creation or annihilation of exciton is possible only close to $K = 0$, i.e., at zone center due to negligible momentum of involved photon, hence at $K = 0$ it is very pronounced transition which broadens with temperature. Due to delta function like density of states and narrow spectral width the excitonic recombination is of particular importance for the laser diode applications [19].

Besides free excitons, excitons bound to shallow impurities play an important role for the optical properties close to the band-edge of ZnO at low temperatures [18, 21]. A free exciton can combine with the impurity or defects to form bound exciton. For example, a free exciton can combine with a donor or acceptor impurities (neutral or ionized) to form a donor or acceptor like bound excitons. The binding energy of the bound exciton is much smaller than that of the free exciton; therefore, they are observed at very low temperatures. Both the free and the bound excitons may occur simultaneously in the semiconductor and can be differentiated by their energy positions and line widths [18, 21]. The energy level of the bound exciton is below the free exciton energy by an amount equal to the binding energy of bound exciton and can be given by the following equation:

$$h\nu = E_g - E_B - E_D \quad (3.6)$$

where E_g , E_B , and E_D are the bandgap and binding energy of free and bound excitons, respectively. The energy position of the bound excitons is also shown in Fig. 3.1b. The bound excitonic transitions are characterized by extremely narrow spectral width and are generally observed at low temperatures [18]. With increasing temperature, the bound excitons disappear due to thermal dissociation of excitons from the defect complexes. Like free excitons, the bound excitons can also recombine by emission of one or more LO phonons, however the interaction of LO phonons with bound excitons is generally very weak.

3.2.2 LO Phonon Replicas and Deep Level Transitions

In polar semiconductors such as ZnO, one of the channels of the excitonic recombination is through mediation of optical phonons [2, 18, 21]. In ZnO with partial ionic bonding, a long-range polarization field is created due to the vibration of cation and anion against each other in longitudinal mode. This results in strong scattering of LO phonons with excitons and modifies the optical recombination and emission characteristics especially at elevated temperatures [21]. In such cases, the excitons recombine by emission of one or more LO phonons as the LO phonons are possible at $K = 0$. Hence the narrow emission spectrum of exciton is replicated at several lower photon energies represented as [21]:

$$h\nu = E_g - E_{ex} - mE_p \quad (3.7)$$

where m is the number of optical phonons involved and E_p is their energy. Like free excitons, the bound excitons can also recombine by emission of one or more LO phonons; however, the interaction of LO phonons with bound excitons is generally very weak.

Other than band to band transitions of excitons and their phonon replicas, which are responsible for the VU-Blue PL, there are also mid-gap PL emissions from ZnO in the visible spectral region. These recombination processes occur due to the formation of donor, acceptor, or other structural defect related states in ZnO bandgap. The various downward electron transitions responsible for yellow, blue, green, and red luminescence observed in ZnO are found to be due to (a) deep acceptor defect levels (b) shallow Oxygen vacancy induced defect levels, (c) Singly ionized Oxygen vacancies induced defect levels, and (d) Zn interstitials induced defect levels. Depending on the defects and other conditions prevailing in the sample to be investigated and the measurement parameters, PL transition corresponding to some or all of the above-mentioned mechanisms are observed.

3.2.3 Effect of Quantum Confinement

The quantum confinement effects in low dimensional ZnO structures modify its optical properties significantly. A confined structure is the one, which has one or more of its dimensions reduced to the size of confinement regime, i.e., of the order of de Broglie wavelength, which is normally in nanometers. If the confinement occurs in one dimension only (say z direction) and the charge carriers have free motion in other two directions (x and y), such a structure is known as two dimensional (2D) quantum structure or a quantum well. In practice, a quantum well consists of a low bandgap semiconductor layer flanked by two layers of a higher bandgap semiconductor of nearly similar crystal structure on either side. These layers are called the barrier layers and are invariably thicker than the confinement layer, which is of thickness in the nanometer regime. In this case, the motion of the charge carriers is restricted along the film thickness (z direction) due to potential barriers created by high bandgap semiconductor layers and has two degrees of freedom.

The energy states of charge carriers in semiconductor quantum structure of different dimensionality can be calculated by solving the Schrödinger equation with appropriate boundary conditions. The energy of charge carriers in three dimensions is the sum of the kinetic energy due to its free motion in all the three dimensions and can be represented with following expression in usual terms:

$$E_{\text{Total}}^{3D} = \frac{\hbar^2}{2m} (k_x^2 + k_y^2 + k_z^2) \quad (3.8)$$

In case of 2D quantum wells and under infinite potential well approximation, the total energy of the electron, which is the sum of quantized energy (in confined direction z) and the kinetic energy due to its (x, y) motion (in unconfined directions) is given as:

$$E_{\text{Total}}^{2D} = En_z + \frac{\hbar^2}{2m} (k_x^2 + k_y^2) \quad (3.9)$$

where En_z is the energy of electron in the confinement direction and can be expressed as:

$$En_z = \frac{\hbar^2}{2m} \left(\frac{n_z \pi}{a} \right)^2 \quad (3.10)$$

where \hbar is Planck's constant, a is the size of the well in the confinement direction, and n_z is quantum number having values $n_z = 1, 2, 3, \dots$

It is obvious from Eq. 3.10 that quantum confinement results in discreteness of the energy levels, which are dependent on the size of the confinement dimension. The energies and wave functions for the first two quantized states of a quantum well are shown in Fig. 3.2. A blue shift in the semiconductor's bandgap is a natural consequence of the quantization of energy levels, which increases with decreasing size. A similar size dependence of the energy states can also be expected for holes in the valance band.

If the barrier potential is finite, the wave function decays exponentially into the barrier region and is a Sine or Cosine function in the quantum well. By matching the wave function and its derivatives at the boundaries, the energy and wave function can be obtained by the solution to the following set of transcendental equations [22, 23] using usual symbols

$$\begin{aligned} \alpha \tan \frac{\alpha \omega}{2} &= \beta \\ \alpha \cot \frac{\alpha \omega}{2} &= -\beta \end{aligned} \quad (3.11)$$

where

$$\alpha = \sqrt{\frac{2m^3 E}{\hbar^2}} \quad \text{and} \quad \beta = \sqrt{\frac{2m^3 (V - E)}{\hbar^2}}$$

V is the finite barrier height and m is the effective mass of carriers. These equations can be solved numerically to get the energy and wave function for a 2D quantum wells with finite barrier heights.

The size confinement also modifies the excitonic behavior discussed in Sect. 3.2.1. The excitonic binding energy increases significantly with reducing size of the semiconductor [21–23]. The energy states of free excitons in 2D quantum well structures can be calculated by solving Schrödinger equation including both Coulombic interaction between the carriers and confining potential due to the potential barriers [21, 22], which can be expressed as:

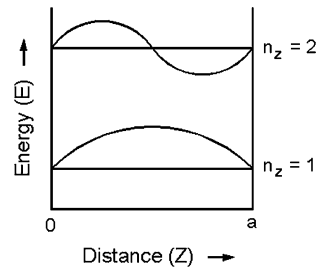
$$E_{\text{ex}}^{2\text{D}} = \frac{E_B}{(n - \frac{1}{2})^2} \quad (n \geq 1) \quad (3.12)$$

where E_B is the binding energy of free excitons in three dimensions (Eq. 3.10) and n is an integer. For $n = 1$ the binding energy of exciton in 2D structures can be given as:

$$E^{2\text{D}} = 4E_B \quad (3.13)$$

Hence binding energy of the exciton in two dimensions increases theoretically ~ 4 times the bulk value. However, experimentally it has been observed that the binding energy varies between E_B to $3 E_B$ due to leakage of the electron wave

Fig. 3.2 Schematic of energy levels and wave functions of electron in a quantum well



function in the barrier region because of finite confining potential. Quantum confinement also modifies the excitonic Bohr radius [21]. The Bohr radius of the exciton in two dimensions can be given as:

$$a_B^{2D} = \frac{a_B^{3D}}{2} \quad (3.14)$$

Hence, the exciton Bohr radius in the 2D quantum well decreases compared to the three dimensional case. Since the relative separation of electron and hole of the exciton reduces in nanostructured semiconductors due to spatial confinement as compared to the three dimensional solid, the oscillator strength of the optical transitions increases significantly in low dimensional semiconductors. However, at sufficiently low thickness of quantum well layer, i.e., well layer thickness much lesser than the excitonic Bohr radius, the excitons behave like bulk excitons. The 0D confinement effect on the excitons is still under intense investigation both theoretically and experimentally. From elementary and also involved theoretical calculations it has been established that excitonic binding energy should enhance further with size in case of 0D structures compared to their 2D and 1D counterparts. However they exist at interesting size regime in which size of the QDs is smaller than the excitonic Bohr radius. It is currently a matter of intense investigation whether the optical transitions in these ultra-small QDs are of excitonic nature or excitons do not exist at all in such structures. Our investigations in this area which are presented in subsequent sections below have given a clue that possibly the optical transitions in such structures are mainly due to unbound electron-hole pairs which are strongly confined and interacting through columbic interaction.

3.3 Photoluminescence Spectroscopy Setup

Photoluminescence spectroscopy is a contactless, nondestructive method of probing the electronic structure of materials and is a useful technique for the characterization of photoemissive processes occurring in materials [18, 21, 24]. Photoluminescence spectroscopy is based upon the principle of measuring the energy distribution of emitted photons due to radiative recombination of free carriers or excitons after optical excitation. In direct bandgap semiconductors, the emission of photon is a reverse process of the absorption. Figure 3.3 shows schematic of the experimental setup for PL spectroscopy. The PL is excited with an intense pump laser beam of photon energy greater than the bandgap of the semiconductor sample which generates free electrons and holes in the conduction and valence bands, respectively, or free excitons. The emitted PL is dispersed with a high-resolution monochromator (MC1) and detected by using suitable detector such as Charge Couple Device (CCD) or photomultiplier tube (PMT). Normally, a PMT is used as a detector to get higher gain while CCD is used to get faster

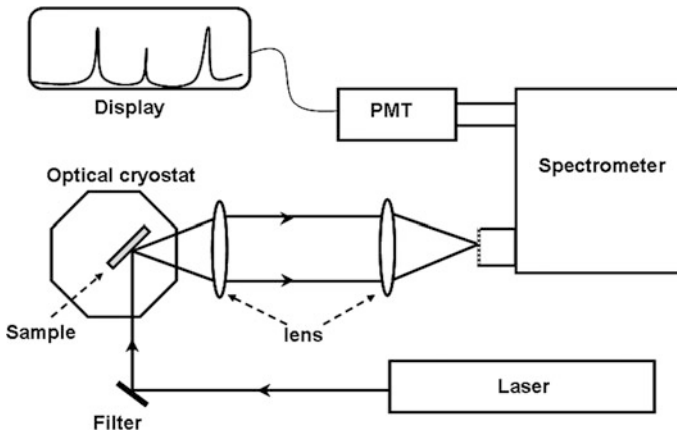


Fig. 3.3 Schematic of the experimental setup of PL spectroscopy

response. In-phase detection of the PL signal is performed with the help of a lock-in amplifier and a mechanical chopper capable of chopping the laser light at desired frequency. A long pass filter is used to block the scattered laser light.

The main strength of the PL spectroscopy technique lies in its sensitivity to detect very weak signal, i.e., high signal-to-noise ratio, which depends on the quality of the sample. It provides a direct measure of the optical quality of the samples and the compositional as well as spatial homogeneity of the epitaxial layers. Its main limitation is a weak or no PL signal for indirect bandgap materials. It provides only the lowest excited state information for quantum structures and requires low temperatures to suppress the luminescence from defects in case of poor quality samples. Photoluminescence technique for semiconductor characterization has achieved significant success and popularity partly due to the simplicity of the technique and the no requirement of sample processing. Photoluminescence signal from a grown structure is directly related to its optical quality needed to make the light-emitting devices. Time-resolved PL spectroscopy provides Information about recombination kinetics, surface recombination, and transport dynamics. Spatially resolved PL spectroscopy is sensitive to sample inhomogeneities and transport processes. Photoluminescence spectroscopy is useful in quantifying, (a) optical emission efficiencies, (b) composition of the material (i.e., alloy composition), (c) impurity content, and (d) quantum size effect etc.

3.4 Photoluminescence Spectroscopy of ZnO Thin Films

We carried out a detailed study of the PL emanating from high-quality ZnO thin films grown on sapphire substrates in the temperature range of 10–300 K to understand various recombination mechanisms and their relative weight on the

light emission from ZnO. Photoluminescence processes due to recombination of free (F_X) and bound (B_X) excitons and associated with the LO phonon mediated transitions were observed and studied as a function of temperature. The results of these studies are presented and discussed in this chapter.

The ZnO thin films, multiple quantum wells, and multilayer matrices of Alumina capped ZnO quantum dots used in this study were grown on epi-polished (0001) Sapphire substrates having rms surface roughness <0.5 nm using pulsed laser deposition (PLD). A third harmonic Q-switched Nd:YAG laser (355 nm, 6 ns, and 10 Hz) was used at a fluence of ~ 2 J/cm² to ablate the ZnO target which was prepared by palletization and sintering of its high purity (99.9995 %) powder. The growth was carried out in high purity (99.999 %) Oxygen ambient at a partial pressure of $\sim 1 \times 10^{-5}$ Torr and at a substrate temperature of ~ 750 °C. Thickness of these films as measured by step profiler was ~ 500 nm. Details of the growth process have been described elsewhere [25, 26]. Crystalline quality of the grown films was studied using Phillips make high-resolution X-ray diffractometer (HRXRD) with a resolution of 0.05° which revealed highly crystalline and c-axis oriented growth [25, 26] with c-axis lattice parameter of ~ 5.209 Å in close agreement with the reported bulk value of 5.20661 Å [27], indicating nearly strain-free films. The full width at half maxima (FWHM) of ω -rocking curve of (0002) ZnO peak was $\sim 0.11^\circ$ which compared favorably with the value of $\sim 0.13^\circ$ reported earlier by Ohtomo et al. [28]. The Φ -scans of HRXRD revealed 30° in-plane rotated growth of ZnO lattice on Sapphire when grown at 750 °C in conformity to the strain free nature of the films [25, 26].

The temperature-dependent PL measurements were carried out in the range of 10–300 K using a 20 mW He–Cd laser operating at 325 nm as an excitation source [27]. The PL signals were recorded by a photomultiplier tube in photon counting mode after dispersing it through a 1 m long monochromator. Figure 3.4 shows the PL spectrum from ZnO film in broad spectral energy range of 1 to 4 eV at 10 K. A strong luminescence in the UV region at around 3.35 eV, corresponds

Fig. 3.4 PL spectrum from ZnO film at 10 K in broad spectral range of 1–4 eV

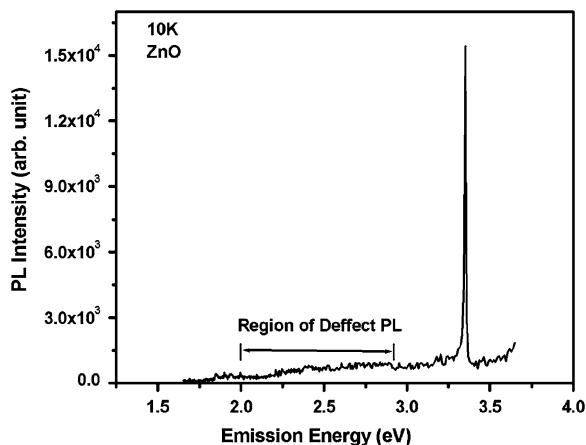
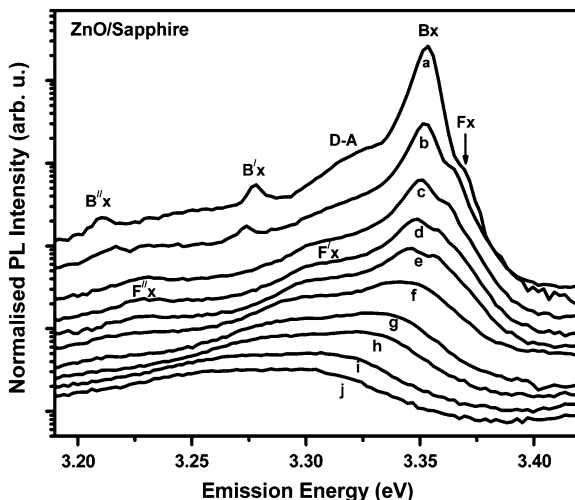


Fig. 3.5 PL spectra of ZnO thin film taken at different temperatures **a** 10, **b** 50, **c** 70, **d** 90, **e** 110, **f** 150, **g** 190, **h** 210, **i** 250, and **j** 300 K. The spectra are plotted in logarithm scale, multiplied and vertically displaced for clarity

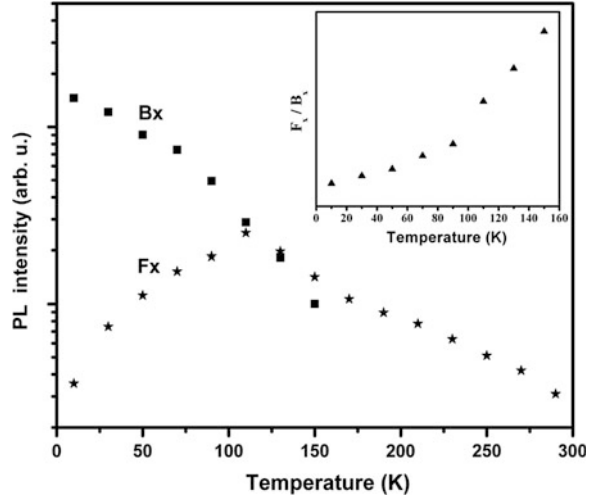


to ZnO bandgap due to excitonic recombination. It is interesting to note that the deep level emission in the visible spectral region, which is considered to be due to off stoichiometry, i.e., oxygen vacancies, zinc interstitial, and other structural defects is almost negligible, indicating nearly defect free and stoichiometric growth of ZnO on sapphire. However, the strong near band-edge emission in UV spectral region has fine structures containing various peaks which changed their position and intensity with temperature. To get deeper insight of the PL processes occurring in ZnO, we have carried out the PL measurements at different temperatures in the broad temperature range from 10 to 300 K.

Photoluminescence spectra of a ZnO film recorded at different temperatures in the range of 10 to 300 K are shown in Fig. 3.5. As can be seen in this figure, the PL spectra contained various emission features, corresponding to different recombination mechanisms of excitons. To determine the individual peak positions and its intensity within a spectrum, we reconstructed the spectrum using multiple standard Gaussian profiles. It can be seen that at low temperatures the near band-edge emission was dominated by radiative decay of donor bound excitons (B_X) that peaked at ~ 3.357 eV at 10 K with a line width of ~ 6 meV as commonly observed in the low temperature PL of ZnO [1, 21, 29–31]. The PL spectral feature from the free exciton recombination (F_X) at ~ 3.374 eV appeared as a shoulder with intensity almost two orders of magnitude smaller than that of the bound exciton emission. It is also evident that the intensity of the F_X peak increases at the expense of B_X peak with increase in temperature and finally disappears.

To understand the temperature dependence of the F_X and B_X peaks, the respective PL peak intensities were plotted as a function of temperature which is shown in Fig. 3.6. As seen in this figure, the B_X peak intensity decreases rapidly with increasing temperature and disappears completely at ~ 130 K in the background of F_X ; however, the F_X peak intensity initially increases steadily with temperature from 10 to ~ 110 K and then gradually decreases up to 300 K. The rapid decrease in the

Fig. 3.6 PL peak intensity of bound excitons (B_X) and free excitons (F_X) as a function of temperature. The inset shows the variation of the ratio (F_X/B_X) with temperature



intensity of B_X and monotonic increase in the intensity of F_X with temperature up to 130 K can be attributed to the enhanced thermal dissociation of bound excitons into free excitons with increasing temperature [21, 30, 31]. Accordingly, the ratio of PL peak intensity of F_X and B_X increased monotonically with increasing temperature in the range of 10–300 K. This is explicitly shown in the inset of Fig. 3.6. The temperature-dependent quenching of B_X and F_X intensity can be used to estimate their activation energy using the following equation:

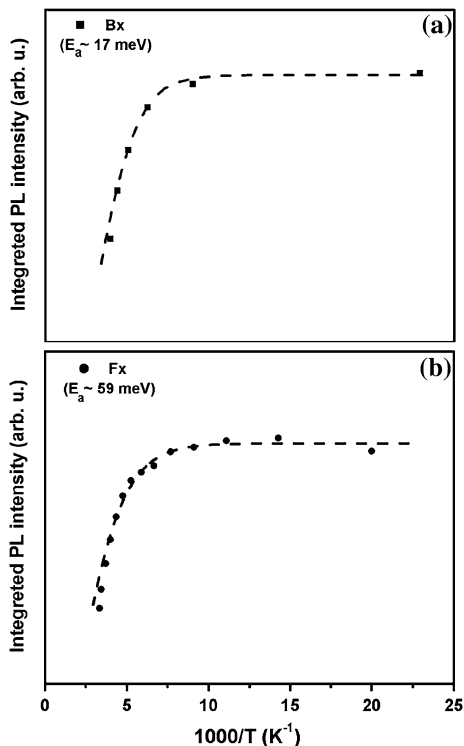
$$I(T) = I_0/[1 + A \exp(-E_a/k_B T)] \quad (3.15)$$

where E_a is the activation energy of the thermal quenching process, k_B is Boltzman constant, T is temperature, I_0 is the integrated intensity of B_X at 0 K, and A is a constant.

Figure 3.7a, b shows the natural logarithm of the integrated intensity of B_X and F_X as a function of $1000/T$. From a fit to the experimental data as shown by solid line in Fig. 3.7a, E_a for bound exciton was estimated to be ~ 17 meV, consistent with the binding energy obtained from the difference in the B_X and F_X peak positions at 10 K and reported values of binding energy (10–20 meV) of donor-bound exciton complexes in case of bulk ZnO [29–31]. Similarly, the binding energy of the exciton was estimated to be ~ 59 meV closely matching with the theoretical value.

In addition to the near band-edge excitonic emissions at 10 K, two other weak features in the PL spectrum shown in Fig. 3.5 are at ~ 3.284 and ~ 3.214 eV. These peaks are ~ 72 and 144 meV away, respectively, from the B_X peak as can be seen in Fig. 3.5. These approximately equidistant PL features could be attributed to the 1 and 2-LO phonon-mediated recombination of the bound excitons [21] and are represented by B'_X and B''_X , respectively. However, the PL peak intensities of B'_X and B''_X quenched more rapidly with temperature compared to that of the B_X

Fig. 3.7 Integrated PL intensity of the **a** B_X and **b** F_X as a function of $1000/T$. The plotted data was fitted using Eq. 3.15 as shown by broken line to estimate respective activation energies

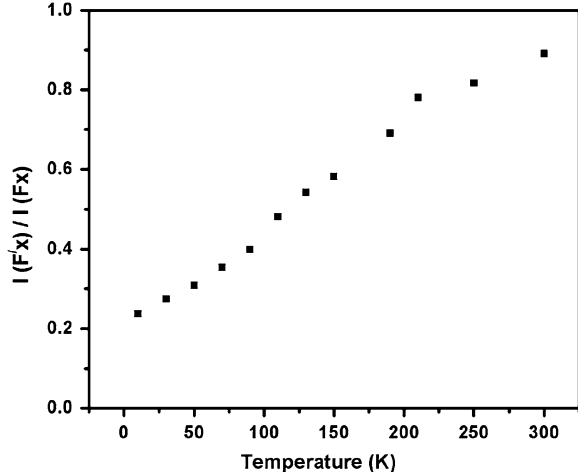


and they disappeared at ~ 70 K. The broad emission feature at ~ 3.32 eV located between the bound exciton emission and its 1-LO phonon replica at 10 K which quenched rapidly with temperature and disappeared at ~ 50 K, has been attributed to the recombination arising from the donor-to-acceptor pair transitions [27, 30, 32]. However with increasing temperature beyond 50 K, two other PL peaks due to 1 and 2 LO phonon-mediated recombination of free excitons represented by F'_X and F''_X , respectively appeared. The intensity of these PL peaks increased gradually relative to F_X with increasing temperature as seen in Fig. 3.5.

Figure 3.8 shows the variation of the ratio of the PL peak intensity of F'_X and F_X . It can be seen that this ratio increases monotonically close to unit with increasing temperature up to RT.

At RT, the dominant transitions were found to be due to F_X and F''_X . The line width of the F_X at RT was found to be ~ 93 meV which is lower than the reported value of ~ 117 meV for ZnO grown on Sapphire by MBE [33] and ~ 120 meV by MOCVD [34]. The deep level emission in ZnO, which has been attributed to the crystal defects [35] such as oxygen vacancies, zinc interstitials, and oxygen anti-sites was negligible in our case, both at low and room temperatures. Narrow width of the free excitonic PL peak at RT along with the negligible deep level emissions are clear indications of high structural and optical qualities of the ZnO films grown by PLD.

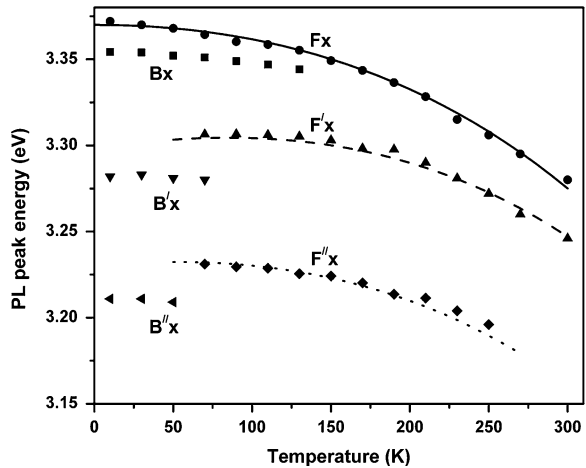
Fig. 3.8 Variation of ratio of intensity of free exciton and its first LO phonon replica as a function of temperature



Temperature dependence of the spectral position of various PL peaks from the ZnO film is shown in Fig. 3.9. It can be seen that peaks corresponding to B_X and F_X and their associated phonon replicas are monotonically red shifted with increasing temperature at different rates. The shift in the exciton energy essentially results from the bandgap shrinkag and thermal dissociation of bound excitons assuming that exciton binding energy is independent of temperature. The dependence of the bandgap on temperature can be explained using the well-known Varshni's empirical relationship [27] as follows:

$$E(T) = E(0) - \frac{\alpha T^2}{\beta + T} \tag{3.16}$$

Fig. 3.9 Temperature dependence of energy positions of F_X , B_X , F'_X , B'_X , F''_X , and B''_X PL peaks. Solid line shows the fit to the F_X peak values according to Varshni's empirical relation. Dashed and dotted lines show the fit to the F'_X and F''_X considering free exciton kinetic energy



where $E(0)$ is the bandgap of the material at 0 K, α and β are the fitting parameters, and β is related to the Debye temperature θ_D . If we assume binding energy of the exciton to be independent of temperature, then the same Eq. 3.16 can be used to explain the temperature-dependence of energy state of the free excitons. The best fit to the experimental data for the F_x peak of ZnO film, as shown by the solid lines in Fig. 3.9 was obtained for $\alpha = 8.2 \times 10^{-4}$ eV/K and $\beta = 1070$ K and $E(0) \sim 3.38$ eV [28].

However, the B_X peak position is red shifted gradually with temperature compared to F_X and hence the separation (F_X-B_X) reduced from ~ 17 to ~ 11 meV with increasing temperature from 10 to 130 K. The observed decrease in the separation (F_X-B_X) with temperature can be explained considering the excitonic fine structure in bulk single crystals of ZnO [36]. According to this finding, the emission band due to recombination of bound excitons in bulk ZnO is composed of many closely spaced transitions associated with various unintentionally introduced donors and/or donor like defects. The relative intensities of these emission peaks depend upon the temperature and nature of defects [37]. We suggest that with increase in temperature from 10 to 130 K the bound excitons at 10 K with activation energy of ~ 17 meV dissociate and transform into bound excitons associated with shallow donor defects. This leads to the successive population of shallow donor bound exciton states with comparatively less binding energy as the temperature is increased. Therefore, a decrease in the separation (F_X-B_X) with increasing temperature is observed. The observed values of the separation (F_X-B_X) at different temperatures in the range of 10–130 K are in good agreement with the reported values of binding energies of donor bound exciton complexes which lie in the range of ~ 10 –20 meV [30, 36].

The energy separation between the PL peaks F_X and its LO phonon replica F'_X , which is the characteristic energy of the LO phonon in ZnO (~ 72 meV) showed an unusual temperature dependence. It can be seen from Fig. 3.9 that the PL energy position of F'_X (first phonon replica of F_X) show much stronger temperature dependence than F''_X (second phonon replica of F_X) and F_X in the range of 50–300 K and the separation between the F_X and F'_X , i.e., ($F_X-F'_X$) was found to decrease more rapidly than the separation between the F_X and F''_X , i.e., ($F_X-F''_X$). The strong temperature dependence of energy separation between the F_X and its LO phonon replicas could be attributed to following two mechanisms (i) shift in the energy of phonon with either temperature [38] and/or stress [39] and (ii) due to the increase in kinetic energy of the free excitons with temperature [21].

The phonon energy in solids is known to decrease with increasing temperature due to thermal expansion of the lattice and can contribute to the observed temperature dependence of the energy separations in the present case [38]. The change in the energy of the LO phonons in ZnO films with increasing temperature up to RT was calculated using the formulation of Alim et al. [38] taking into account the thermal expansion and anharmonic coupling effects. All the required parameters were taken from the same Ref. [28]. The estimated shift of LO phonon energy due to change in the temperature from 10 to 300 K was as small as ~ 1.7 meV and

hence inadequate to explain the observed temperature dependence of energy separation. Similarly the change in the LO phonon energy in ZnO film due to residual strain is also negligible as the HRXRD measurements revealed nearly strain free ZnO films on sapphire.

The other possible factor responsible for the observed behavior is the exciton-phonon coupling mechanism. According to the paradigms of Permogorov's [40] and Klingshirn [21], which deal with the asymmetric spectral shape of the phonon-assisted luminescence in polar semiconductors taking into account the kinetic energy of the free excitons, a general relationship for the energies of the emission lines involving phonons and excitons could be written as:

$$F_X^n = F_X - n\hbar\omega_{LO} + \Delta E \quad (3.17)$$

where F_X^n is the energy position of the spectral peak corresponding to the n th phonon replica, F_X is the free exciton energy at $K = 0$, h is the Planck's constant, and ω_{LO} is the LO phonon energy which is ~ 72 meV. The term ΔE is related to the kinetic energy of the gas like free excitons in the crystal [21]. Since the excitons with kinetic energy ΔE move away from $K = 0$ in E - K space, therefore they require mediation of phonons of suitable energy and momentum to recombine. The transition probability of excitons with kinetic energy ΔE is proportional to $(\Delta E)^L$ where L is an integer and hence the kinetic energy of excitons can be approximated to $(L + 1/2)KT$ where the integer L is 0 or 1 [21]. Therefore the energy separation between the free exciton peak and its n th LO phonon replica can be represented in terms of usual and predefined symbols as:

$$F_X^n = F_X - n\hbar\omega_{LO} + \left(L + \frac{1}{2}\right)KT \quad (3.18)$$

The best fit to the observed temperature dependence of the energy position of F'_X peak was obtained for $L = 1$ resulting in a slope of $\sim -3/2 KT$, which is shown by the dashed line in Fig. 3.9. For F''_X , a reasonable fitting of the experimental data, as shown by the dotted line in Fig. 3.9, was obtained for $L = 0$ indicating that the transition probability was independent of the excitonic kinetic energy in this case. The insignificant variation with temperature in the energy of B'_X and B''_X compared to that of F'_X and F''_X seen in Fig. 3.9 indicates that there is a significant difference in the scattering mechanisms between free excitons-phonons and bound excitons-phonons.

3.5 Photoluminescence Processes in ZnO Quantum Wells

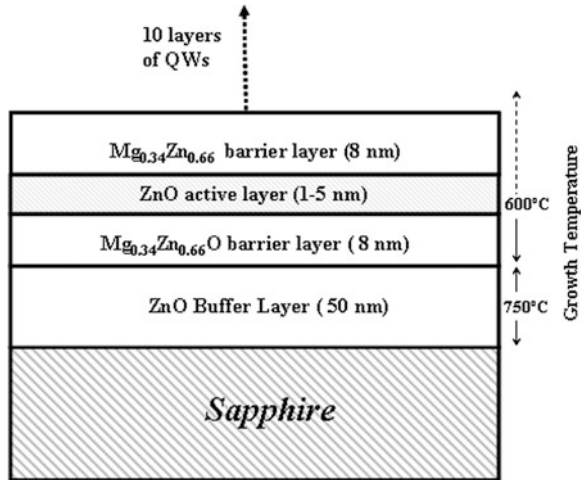
Research and studies on ZnO quantum wells is important for the development of next generation nanophotonic and electronic devices [41, 42]. In general, quantum structures exhibit fascinating size-dependent physical properties such as large oscillator strength of optical transitions, enhanced excitonic binding

energy, tunability of operating wavelength, very low threshold of lasing, and quantum transport properties. The ZnO quantum structures are also ideal systems for studying the effect of dimensionality on the excitonic recombination mechanisms. The nonlinear optical response such as third-order nonlinear susceptibility can be enhanced significantly in ZnO nanostructures compared to that of bulk due to confinement effects [2].

We carried out studies on the PL processes in one dimensional confined structure of ZnO such as multiple quantum wells (MQWs), which are important for the development of modern optoelectronic devices based on quantum confinement effects. Since the excitonic Bohr radius for ZnO is ~ 2.1 nm, the size-dependent quantum confinement effects in ZnO nanostructures can be observed only if the size of structures is less than ~ 4.2 nm. We have accomplished the growth of high-quality ZnO/Mg_xZn_{1-x}O MQWs with well layer thickness in the range of ~ 4 to 1 nm on (0001) on sapphire substrates by using PLD under optimized conditions and observed size-dependent blue shift in ZnO bandgap due to the quantum confinement effect. To the best of our knowledge, we have observed for the first time, efficient luminescence at room temperature (RT) from these MQWs grown on sapphire substrates [43].

Growth of ZnO multiple quantum wells was carried out on sapphire substrates using pulsed laser deposition technique. It is well known that the ZnO/Mg_xZn_{1-x}O hetero interfaces are stable below 650 °C [44]. However the high crystalline quality of ZnO and its alloys can be achieved at high growth temperature of 750 °C and above due to 30° rotated growth with respect to sapphire through domain epitaxy as discussed in Refs. [26, 27, 45]. To accomplish these contradictory growth requirements, we evolved a buffer-assisted growth methodology [26] wherein a ZnO buffer layer of ~ 50 nm thickness was first grown on Sapphire substrate at 750 °C and the subsequent growth of barrier and well layers was carried out on this ZnO template at a lower temperature of ~ 600 °C. This ensured a high crystalline quality of the barrier and well layers along with the physically and chemically sharp interfaces. Ternary alloy Mg_{0.34}Zn_{0.66}O film with bandgap of ~ 4.1 eV at room temperature was deposited using sintered pellet of MgZnO as barrier layer. Depositions were carried out at a laser fluence of ~ 0.6 J/cm² by sequentially ablating the ZnO and MgZnO targets mounted on a multi-target carousel in the PLD chamber. The growth chamber was initially evacuated to a base pressure of $\sim 1 \times 10^{-7}$ Torr using a Turbo Molecular Pump and depositions were carried out in high purity (99.9995 %). Oxygen ambient at a partial pressure of $\sim 1 \times 10^{-5}$ Torr. The typical growth rate at this fluence, which was measured in separate experiments, was found to be ~ 0.1 nm/s for ZnO and ~ 0.08 nm/s for MgZnO targets, respectively. These growth rates were subsequently used to determine the barrier and well layer thicknesses. Ten periods of ZnO/Mg_xZn_{1-x}O layers were grown with a constant Mg_xZn_{1-x}O barrier layer thickness of ~ 8 nm and variable thickness of ZnO well layer in the range of ~ 1 to 4 nm in separate MQWs. The schematic of the ZnO MQWs grown by us is shown in Fig. 3.10. The Mg concentration in the Mg_xZn_{1-x}O barrier layer was found to be ~ 34 % using Energy Dispersive X-ray Analysis.

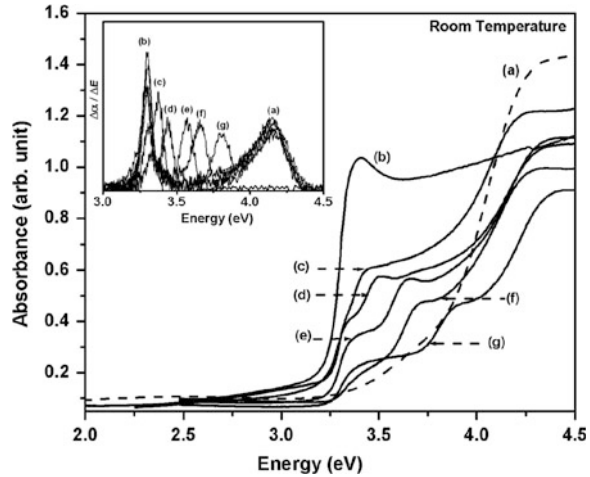
Fig. 3.10 Schematic of the ZnO/Mg_xZn_{1-x}O multiple quantum wells



The optical properties of the ZnO multiple quantum wells were studied using an absorption photo-spectrometer (SHMADZU, UV-3101PC) at room temperature and temperature dependent PL spectroscopy. For PL measurements a 5 mW He–Cd laser operating at 325 nm was used as an excitation source and the resulting luminescence was collected through a $\frac{1}{4}$ m monochromator with a band pass of ~ 0.5 nm in the temperature range of 10 K to RT.

All the MQW samples appeared highly transparent and shining to the naked eyes with an average transmission $\sim 80\%$ in the visible spectral region. Figure 3.11 shows the room temperature optical absorption spectra of these MQWs in the photon energy range of ~ 2 to 5 eV. Absorption spectra of ~ 200 nm thick ZnO and MgZnO thin films directly grown on Sapphire substrate are also shown in the same figure for reference. The latter two spectra show the band-edge of ZnO and Mg_{0.34}Zn_{0.66}O bulk at ~ 3.3 and 4.1 eV, respectively, along with conspicuous excitonic humps. It can be seen from Fig. 3.11 that each absorption spectrum of the MQWs consists of three well resolved features. The broad shoulder at ~ 3.3 eV obviously corresponds to the ZnO buffer layer grown prior to every multiple quantum wells. The shoulder at ~ 4.1 eV corresponds to the absorption due to Mg_{0.34}Zn_{0.66}O barrier layers. It is noteworthy here that the constant position of the absorption edge corresponding to the barrier layers of Mg_{0.34}Zn_{0.66}O in all the MQW samples is indicative of negligibly small inter-diffusion of chemical species at the ZnO/Mg_{0.34}Zn_{0.66}O interfaces. The central peak in these absorption spectra is found to correspond to the $n = 1$ excitonic transition of the ZnO quantum wells. It can be seen that this peak undergoes monotonic blue shift with decreasing well layer thickness from ~ 4 to 1 nm as expected from the size-dependent quantum confinement effect. The band-edge of ZnO/Mg_{0.34}Zn_{0.66}O MQWs at different well layer thicknesses was estimated from their first derivative absorption spectra. The first derivatives of the absorption spectra of the ZnO MQWs with different well layer thicknesses are shown in the

Fig. 3.11 Room temperature optical absorption spectra of **a** 200 nm thick $\text{Mg}_{0.34}\text{Zn}_{0.66}\text{O}$ barrier layer **b** 200 nm thick ZnO layer and ZnO MQWs of different well layer thickness **c** 4, **d** 2.5, **e** 2, **f** 1.5, and **g** 1.0 nm. The corresponding first derivatives of the absorption spectra are shown in the *inset*



inset of Fig. 3.11. The spectra show clear peaks corresponding to the $n = 1$ excitonic transitions, which shift toward shorter wavelength on decreasing the well layer thickness. The bandgap energy of the MQWs of different well layer thicknesses can be obtained from the peak positions in the corresponding first derivative absorbance spectrum.

The PL spectroscopy of ZnO MQWs of different well layer thickness was carried out at different temperatures in the range of 10–300 K to study the optical emission processes in ZnO MQWs. A 5 mW He–Cd laser operating at 325 nm was used as an excitation source. The sample was kept in a close cycle optical cryostat for temperature-dependent measurements. The PL signal was collected through a $\frac{1}{4}$ m monochromator with a band pass of ~ 0.5 nm and was detected by a photomultiplier tube.

Figure 3.12 shows 10 K PL spectra of ZnO MQWs grown on sapphire with different well layer thickness along with 200 nm thick ZnO layer. The PL from $\text{Mg}_x\text{Zn}_{1-x}\text{O}$ barrier layers and 1 nm thick ZnO MQW could not be observed because their bandgap which was estimated to be ~ 4.1 and 3.8 eV, respectively, at room temperature from their absorption spectra exceeded the energy of the excitation photons from the He–Cd laser. A weak PL from the underlying ZnO buffer layer was indeed observed at ~ 3.37 eV in each sample but not shown in the graph. It can be seen that as the well layer thickness was decreased from ~ 4 to 1.5 nm the PL peak shifted from ~ 3.41 to ~ 3.78 eV in line with size-dependent quantum confine effects. It can also be seen that the line width of the PL peaks increases with decreasing well layer thickness. The broadening of PL peak with decreasing well layer thickness was attributed to fluctuations in well layer thickness within the MQW structures, which increased as the well layer thickness was decreased.

To measure the PL spectra of ZnO MQWs having well layer thickness less than 1.5 nm, we have used an ArF excimer laser operating at 193 nm. Figure 3.13 shows the 10 K PL spectra of ZnO MQW having well layer thickness 1, 1.2, and 1.8 nm respectively [45]. The 1.2 and 1.8 nm thick MQWs were also grown by us

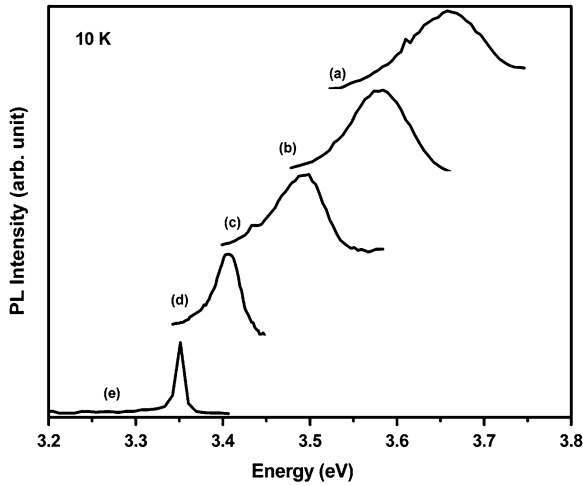


Fig. 3.12 10 K PL from ZnO MQWs of different well layer thickness **a** 1.5 nm, **b** 2 nm, **c** 2.5 nm, **d** 4 nm, and **e** 200 nm thick ZnO film

but not included in absorption spectra shown in Fig. 3.11 for the sake of clarity in the graph. It can be seen from Figs. 3.12 and 3.13 that bandgap of ZnO MQWs shifts toward blue with decreasing well layer thickness up to 1 nm due to quantum confinement effect.

The dependence of bandgap on the well layer thickness of ZnO MQWs is explicitly shown in Fig. 3.14, wherein the bandgap values obtained from 10 K PL

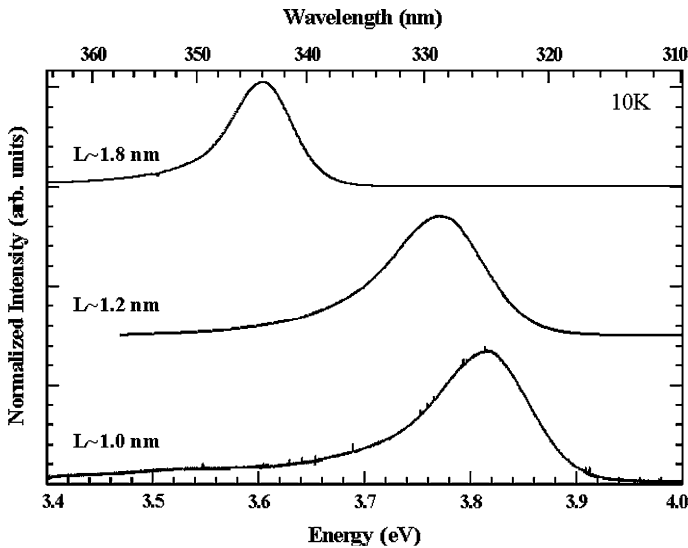
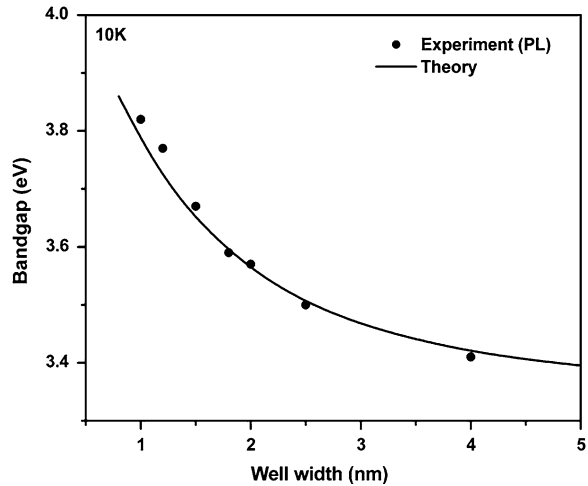


Fig. 3.13 10 K PL from ZnO MQWs with well layer thicknesses down to 1 nm

Fig. 3.14 Bandgap of ZnO MQWs obtained from 10 K PL measurements as a function of well layer thickness



spectra of different MQWs excited using either He–Cd or ArF lasers are plotted as a function of active layer thickness. To understand this dependence, we calculated the QW bandgap at different well layer thicknesses at 10 K by solving the time-independent Schrödinger equation using finite square potential well approximation as discussed in previous Sect. 3.2.3. The binding energy of excitons was assumed to be constant with respect to temperature and well layer thickness. The calculated values are shown by the continuous curve in Fig. 3.14, which shows a reasonable agreement with the experimental values obtained from PL measurements.

Fig. 3.15 PL spectra of ZnO MQWs at a constant well layer thickness ~ 2.5 nm at four different temperatures up to room temperature

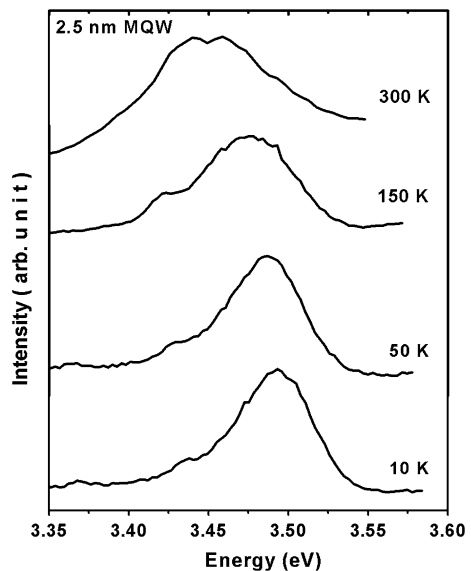
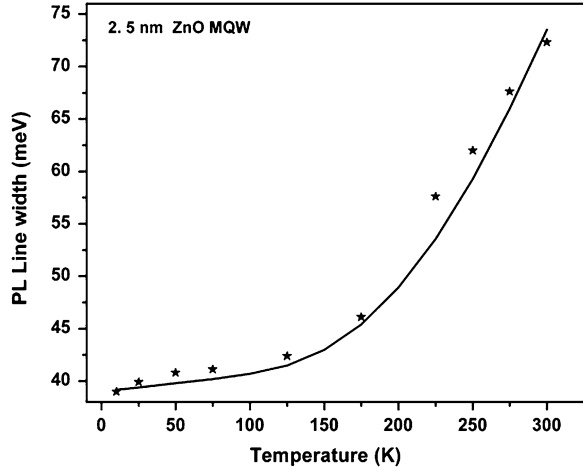


Fig. 3.16 Variation of PL spectral line width with temperature from ZnO MQWs of well layer thickness of ~ 2.5 nm. Solid line shows the fitted theoretical dependence

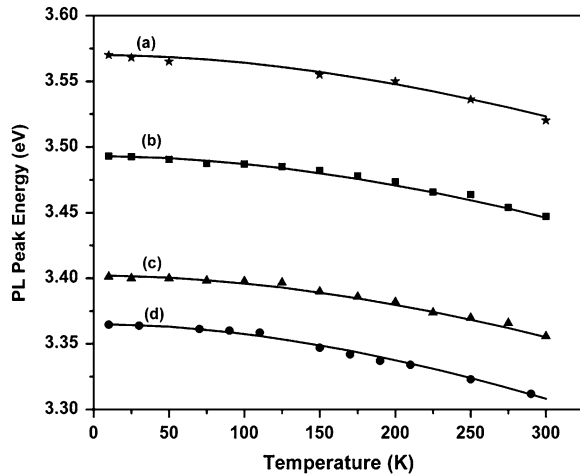


The temperature dependence of PL spectra from ZnO MQWs with a particular well layer thickness of ~ 2.5 nm is shown in Fig. 3.15 for four different temperatures down to RT. It can be seen that the PL peak position shifts toward red and its line width increases gradually with increase in temperature up to RT. The temperature dependence of the FWHM of the excitonic emission peak for a 2.5 nm thick ZnO MQW is shown in Fig. 3.16. It can be seen from Fig. 3.16 that the line width of the PL peak increases gradually up to ~ 120 K and then exponentially up to RT. The temperature-dependent broadening of the PL peak has been interpreted in terms exciton-phonon scattering in different temperature regimes using theoretical formulation developed by Hellmann et al. [46] and O'Neill et al. [47], which is as follows:

$$\Gamma(T) = \Gamma_{\text{inh}} + \gamma_{\text{ph}}T + \frac{\Gamma_{\text{LO}}}{\exp\left(\frac{\hbar\omega_{\text{LO}}}{kT}\right) - 1} \quad (3.19)$$

where $\hbar\omega_{\text{LO}}$ is the LO phonon energy, Γ_{inh} is the inhomogeneous line width at 0 K, γ_{ph} is the coupling strength of exciton-acoustic phonon interaction [46], Γ_{LO} is the parameter related to the strength of exciton-LO phonon coupling [47], and $\exp[(\hbar\omega_{\text{LO}}/kT)-1]^{-1}$ is the population of LO phonons of energy $\hbar\omega_{\text{LO}}$ at temperature T . The dotted line in Fig. 3.16 shows the fitted result based on the O'Neill and Hellmann formulations. The best fit was obtained for the parameter values of $\Gamma_{\text{inh}} = 39$ meV, $\Gamma_{\text{LO}} = 450$ meV and $\gamma_{\text{ph}} = 160$ $\mu\text{eV/K}$. As explained through the Hellmann's formulation [46], the gradual increase of the line width in the low temperature regime up to ~ 120 K is attributed to the exciton scattering with the acoustic phonons while the exponential rise at higher temperatures to that with the LO phonons [46]. Because the temperature dependence of the line width in the present case could be explained using O'Neill and Hellmann formulations, meant exclusively for the excitonic transitions, it indicates that all the PL transitions

Fig. 3.17 Temperature dependence of the PL peak position of ZnO MQWs with different well layer thicknesses **a** 2, **b** 2.5, **c** 4 nm, and **d** 200 nm thick ZnO film. Solid lines show the fit to the respective experimental data using the Varshni's relation (Eq. 3.16)

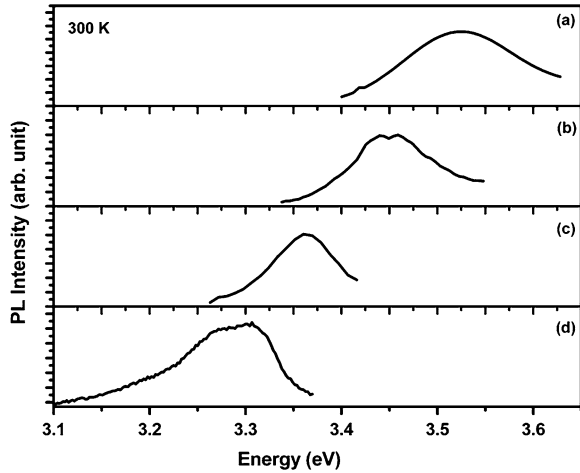


observed in MQWs of different well layer thicknesses up to RT were excitonic in nature [46, 47].

The temperature-dependent PL peak positions for the MQWs with three different active layer thicknesses along with that of ~ 200 nm thick ZnO film are shown in Fig. 3.17. The PL peak positions were found to shift gradually toward red with increase in temperature up to 300 K. The red shift in the semiconductor bandgap with temperature results from the temperature-dependent thermal expansion/dilation of lattice and carrier-phonon scattering. The variation of the bandgap of ZnO MQWs with temperature was studied using Varshni's empirical relation [48] discussed in Eq. 3.16. The best fit to the experimental data for different MQWs, as shown by the solid lines in Fig. 3.17, were obtained for $\alpha = 8.2 \times 10^{-4}$ eV/K and $\beta = 1070$ K where α and β are the fitting parameters [49]. It can be seen from Fig. 3.17 that the MQWs with different well layer thicknesses and 200 nm thick ZnO film show similar functional form of the temperature dependence. The fact that all the MQWs followed the same functional form of the temperature dependence of bandgap, which also matched with that of the 200 nm thick ZnO film, indicates that the strain effects are minimal in these MQWs [50]. The negligible strain effects in these MQWs can be attributed to our optimized high temperature buffer assisted growth scheme which provided 30° in-plane rotated, highly crystalline, smooth, and relaxed ZnO template layers even on the mismatched sapphire substrate [26] for the growth of ZnO quantum structures. The successive low temperature growth of ZnO MQWs over this high temperature grown template layer not only ensured chemically and physically sharp interfaces and smooth surfaces of multilayer structures but also the high structural characteristics.

The room temperature PL spectra of the ZnO MQWs with different well layer thicknesses down to ~ 2 and about 200 nm thick ZnO film are shown in Fig. 3.18. The PL peak intensity for the ZnO MQWs with active layer thickness below 2 nm

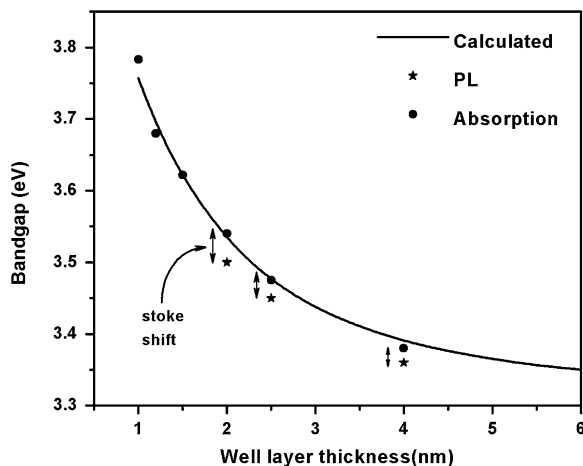
Fig. 3.18 Room temperature PL from ZnO MQWs with different well layer thicknesses of **a** 2, **b** 2.5, **c** 4 nm, and **d** 200 nm thick ZnO film



was negligibly small at RT and hence could not be recorded with the present PL setup. A feeble PL from the underlying ZnO buffer layer was observed (not shown in the figure) at ~ 3.3 eV in each sample. It can be seen in Fig. 3.18 that as the well layer thickness was decreased from ~ 4 to 2 nm, the PL peak shifted from ~ 3.36 to 3.52 eV in line with size-dependent quantum confinement effects. Although there are some reports on the observation of room temperature PL from ZnO MQWs but in these reports lattice match ScMgAlO₄ substrates were used instead of sapphire. To the best of our knowledge, this is for the first time that efficient PL has been observed at room temperature from ZnO MQWs grown on commonly used sapphire substrates [47]. The reduced interface roughness, high crystalline quality along with the minimal strain effects obtained by using high temperature buffer assisted PLD methodology adopted by us appear to be responsible for the observation of an efficient room temperature PL and well resolved absorption edges in RT absorption spectra in these MQWs.

The size-dependence of bandgap obtained from the room temperature absorption and PL measurements of the ZnO MQWs are shown in Fig. 3.19. The bandgap was calculated theoretically at each well layer thickness by solving Schrödinger equation using one dimensional square potential well approximation with finite well depth as discussed in Sect. 3.2.3. The calculated values are shown by the continuous curve in the same figure, which shows a reasonable agreement with the experimental values obtained from absorption spectra as already discussed above. However, the corresponding PL data showed some stoke shift compared to the values obtained from absorption spectra which increased with decreasing well layer thickness. In our views, a clear understanding for such a Stoke shift in ZnO MQWs is not yet well established although some authors have earlier attributed it to the local physical and compositional fluctuations in the barrier layers of ZnO and GaAs [51] MQWs.

Fig. 3.19 Bandgap of ZnO MQWs obtained from room temperature PL and absorption measurements as a function of well layer thickness



3.6 Photoluminescence from Quantum Dots of ZnO

The evolution of next generation photonic devices and sensors etc. necessitated research on ZnO quantum structures. Although a significant amount of research on ZnO-based quantum wells has been reported in the literature; the work on ZnO Quantum Dots (ZQDs) grown on solid substrates is quite scanty. A study on ZQDs grown on solid substrate is important not only to understand the three dimensional quantum confinement effects on the excitonic transitions but also to create new forms of this material which could open more frontiers for its applications. As an example, by growing quantum dots (QDs) one can enhance the linear and non-linear responses in ZnO significantly.

Earlier the ZQDs were grown mainly using wet chemical methods [52–56]. About a decade ago, Ohkubo et al. [57] reported a study on the growth and characteristics of a single layer of ZQDs on atomically flat alumina substrates using PLD technique. To the best of our knowledge, we have grown for the first time, multilayer of ZQDs of varying size by PLD embedded in alumina matrix on optically polished c-axis oriented Sapphire substrates [58–60] and observed size-dependent blue shift in the ZnO bandgap due to 0D quantum confinement effect in line with theoretically calculated values. Recently, there have been a few reports on the PL spectroscopy studies on ZQDs; however, exact details of underlying optical transitions responsible for PL, especially if the dot's size is less than the excitonic Bohr radius, are not yet discussed in detail. We have recently found that some of the PL processes in ZnO dot's size less than the excitonic Bohr radius hereafter called ultra-small QDs show anomalous behaviors compared to their larger counterpart [59]. The basic question which arises from these studies that if at all the excitons exist in such ultra-small QDs? Our experiments suggests that the bandgaps of ultra-small QDs deviate significantly from the excitonic model and the LO phonon coupling with the recombining electron-hole pairs enhances.

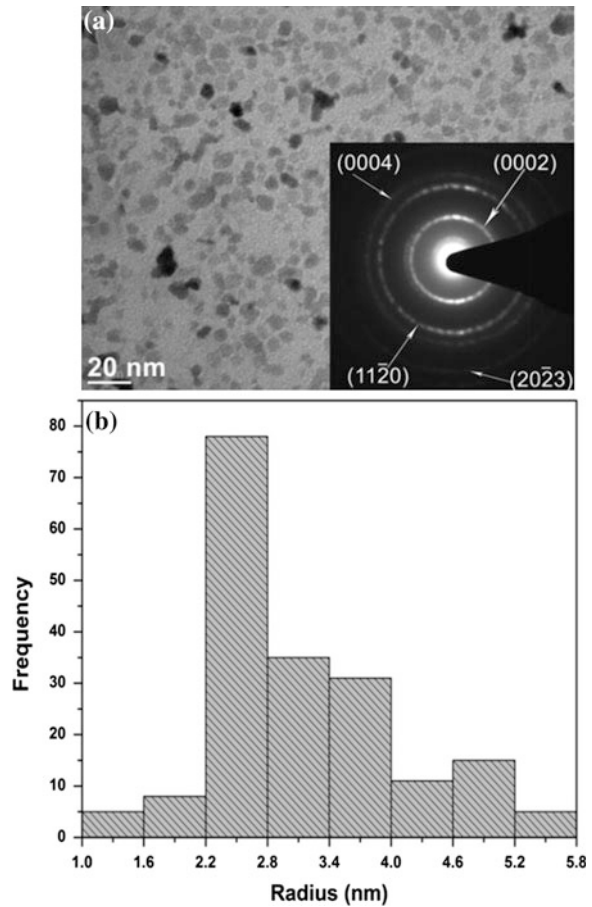
These findings make us propose that excitons may not exist in ultra-small ZQDs and the optical transitions originate from the localized electron-hole pairs. The results of these studies are presented and discussed in the following sections.

Alternate ablation of the sintered targets of ZnO and Al₂O₃ was used to grow a multilayer matrix of alumina capped ZnO nanoparticles. Followed by the deposition of a base layer of alumina on the (0001) Sapphire substrates, 10-layer structure of alternate ZnO nanoparticles and alumina layer was grown at room temperature. While the alumina layer was grown for 120 s in all the samples, the deposition time of ZnO in different samples was varied in the range of ~ 10 to 120 s to grow the nanoparticles of different mean sizes [59]. The deposition of both these materials was carried out at a fluence of ~ 0.6 J/cm² in oxygen ambient at a pressure of about 10^{-2} Torr for good stoichiometry. The optical characteristics of ZQDs were studied using the optical absorption and PL spectroscopy studies of the multilayer structures at room temperature. Size and shape of these QDs were studied using Transmission Electron Microscopy and Atomic Force Microscopy. The size-dependent quantum confinement energy was calculated using the effective mass approximation (EMA) to understand the experimentally observed variation of the bandgap with in-plane quantum dot size. Results of these studies are discussed in following sections.

Figure 3.20a shows typical TEM viewgraph of ensemble of the ZQDs wherein it can be seen that these ZQDs are polydisperse and mostly of irregular shape with density of the order of $\sim 10^{13}$ cm⁻². While most of the ZQDs are isolated but at a few locations those are also coalesced. The inset of Fig. 3.20a shows the selected area electron diffraction (SAED) pattern which confirmed that the QDs were composed of ZnO. The presence of speckles in the SAED pattern indicate growth of certain specific planes in the ZQDs which were identified to be (0002), (11 $\bar{2}$ 0), (0004), and (20 $\bar{2}$ 3) from the observed SAED patterns. Although these ZQDs are of irregular shape, we approximated those to be somewhat circular at the base and hemispherical in three dimensions [60] to work out their theory. The size distribution of these ZQDs is shown in the histogram of Fig. 3.20b. From such histograms the mean radii of the ZQDs were calculated. These mean radii were used for correlating the average band-edges of the ensembles of ZQDs with their corresponding mean sizes, which is presented and discussed later.

The normal θ - 2θ X-ray diffraction pattern of the ZQDs of mean radius of ~ 2.3 nm is shown in Fig. 3.21. One can see in this figure the presence of (0002), (0004), and (20 $\bar{2}$ 3) peaks of ZnO with dominant (0002) ZnO peak indicating most of the ZQDs are c-axis oriented hexagonal wurtzite structures. Presence of these peaks and their narrow line width are indicative of good crystalline quality of these ZQDs. Since this XRD pattern is of polydisperse ZQDs, the peak line width is contributed not only by the size of the particles which in present case in the nm regime but also by the large size distribution and crystalline defects of the particles as shown TEM measurements in Fig. 3.20b. Further it is expected that the larger sized ZQDs will contribute more intensity of the diffracted X-rays than their smaller counterparts and hence the peak line width is weighted more in favor of

Fig. 3.20 **a** TEM viewgraph of a typical ensemble of the polydisperse ZQDs grown by pulsed laser deposition. Inset shows the selected area electron diffraction pattern of these dots. **b** Histogram showing size dispersion of the ZQDs. [Reprinted with permission from Kukreja et al. [59]. Copyright 2011 American Vacuum Society]



larger ZQDs. The calculated mean radius of the ZQDs using Debye–Scherrer formula for the dominant (0002) peak of Fig. 3.21 is ~ 5 nm, which is not very off from the mean radius of ~ 2.3 nm measured from the TEM data.

Figure 3.22 shows the room temperature absorption spectra of the multilayer matrices of alumina capped ZQDs of different mean radii. As can be seen these absorbance spectra do not show a series of isolated absorption peaks rather each spectrum, corresponding to a particular growth time and hence a mean size exhibits a broad absorption feature which is expected due to the broad distribution of ZQD sizes and is found to be due to the $1s_e-1s_h$ transition. Average values of the band-edges were obtained from the first derivative of these spectra and plotted as function of mean size of the ZQDs as shown in the inset of Fig. 3.22. It can be clearly seen from these spectra that the band-edge undergoes a monotonic blue shift with decreasing mean size of the ZQDs as expected from the quantum confinement effects [60, 61]. The bandgap of bulk ZnO at room temperature was taken to be ~ 3.3 eV, which is also shown in this figure for comparison. In this

Fig. 3.21 X-ray diffraction pattern of the ZQDs. The weighted mean radius of these dots measured from the TEM data was about 2.3 nm. [Reprinted with permission from Kukreja et al. [59]. Copyright 2011 American Vacuum Society]

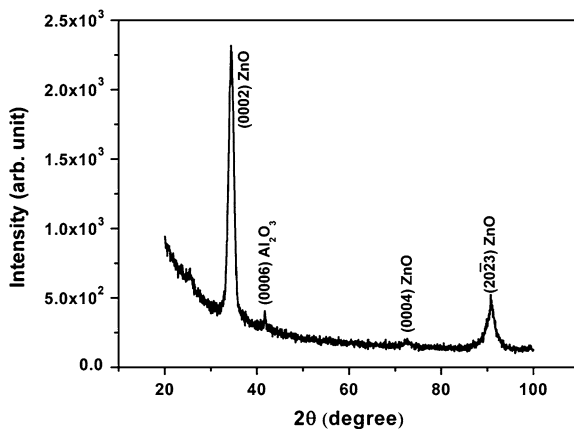
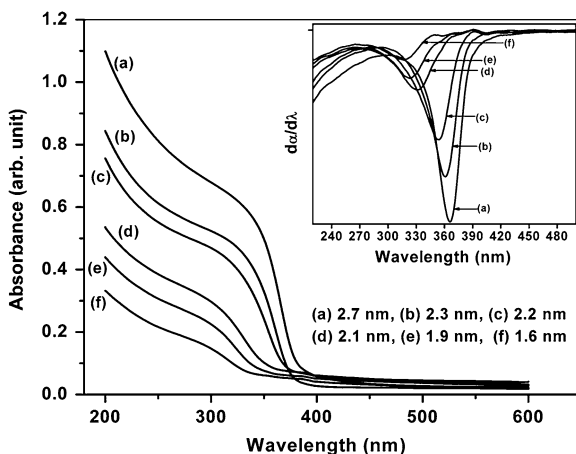


Fig. 3.22 Optical absorption spectra of the ZQDs of different mean radii. Inset shows the first derivative of these spectra. Spectral position of the lowest tip of these derivative spectra was taken as the average band-edge of the ZQDs' ensemble. [Reprinted with permission from Kukreja et al. [59]. Copyright 2011 American Vacuum Society]



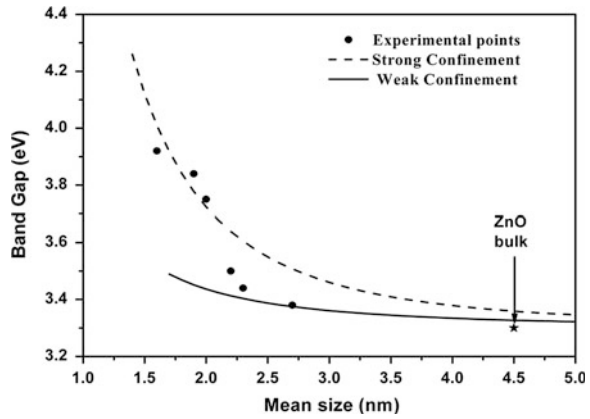
figure, one can clearly see a drastic increase in the bandgap with decreasing size of the ZQDs in the range smaller than the excitonic Bohr radius (a_B) for ZnO which is calculated to be ~ 2.3 nm. In the size range greater than the excitonic Bohr radius, the variation of the bandgap is rather subdued as can be seen in this figure.

To understand these observations in two size-domains, i.e., the dot size shorter than the excitonic Bohr radius and other one with the dot size larger than the excitonic Bohr radius; we have used the effective mass approximation with strong confinement and weak confinement, respectively. In the size domain where the dot size is smaller than the excitonic Bohr radius, it is plausible that the exciton may not exist and therefore holes and electrons will experience a strong confinement with a characteristic reduced mass and a Coulombic interaction term. Therefore, the bandgap under these circumstances was calculated using the following expression [62–64]:

$$E = E_g + \frac{\hbar^2 \pi^2}{2eR^2} \left(\frac{1}{m_e} + \frac{1}{m_h} \right) - \frac{1.786e}{4\pi\epsilon_0\epsilon_r R} - 0.248E_{ex} \quad (3.20)$$

where E is the bandgap of the dots, E_g the bulk bandgap, R the dot size, m_e and m_h the effective masses of electron and hole, respectively. The last term, i.e., $0.248 E_{ex}$ represents the correlation energy, which can be expressed in terms of the excitonic binding energy E_{ex} [62]. We took $m_e = 0.24 m_0$, $m_h = 0.45 m_0$, $E_g = 3.359$ eV, $E_{ex} = 59$ meV, and $\epsilon_r = 6.01$ for ZnO [54–56]. The plot of the Eq. 3.20 is shown in Fig. 3.23 by solid lines. It can be seen that the match between the theoretical curve and the experimental data is reasonably good except for the case of 1.8 nm dots. This is attributed to the extremely low dot density at this deposition time and therefore a large scatter in the experimental data.

Fig. 3.23 Variation of average band-edge of the ZQDs' ensemble as a function of the mean radius. Experimental data are shown by filled circles while the fitting curves are plots of theoretically calculated values. The location of bandgap of bulk ZnO is also shown. [Reprinted with permission from Kukreja et al. [59]. Copyright 2011 American Vacuum Society]

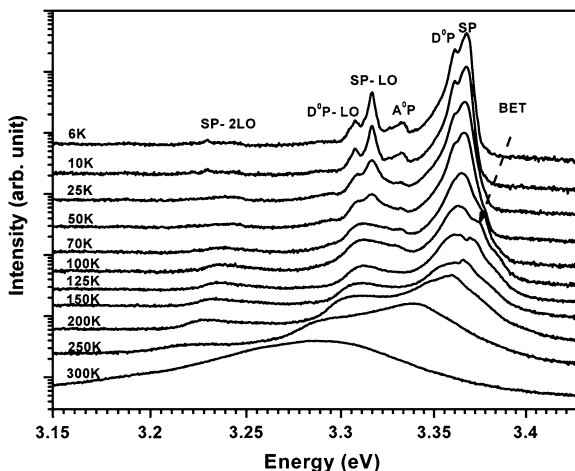


In case of the dot size greater than the excitonic Bohr radius, the excitons can exist and therefore the Coulombic interaction term is replaced by the excitonic binding energy. Further, since the exciton is free to move in the dot, we need to take the translational mass in place of the reduced mass in Eq. 3.21. Thus in weak confinement region, the bandgap of the ensemble of the dots is calculated using the following expression [62]:

$$E = E_g + \frac{\hbar^2 \pi^2}{2eMR^2} - E_{ex} \quad (3.21)$$

where M is the translational mass of the exciton, which is the algebraic sum of the electron and hole effective masses, and R is the mean dot size. As can be seen here that the blue shift in the bandgap as a function of R in this case is much weaker than in the previous case of the strong confinement. A plot of the Eq. 3.21 is also shown in Fig. 3.23. Thus it can be seen in Fig. 3.23 that while the measured band-edge of the ZQDs of mean size of ~ 2.7 nm lies on this curve, the band-edges for ZQDs of sizes ~ 2.3 nm and shorter which we call ultra-small ZQDs tend to

Fig. 3.24 PL spectra of the ZQDs' ensemble of mean radius of about 2.3 nm at different temperatures. [Reprinted with permission from Kukreja et al. [59]. Copyright 2011 American Vacuum Society]



deviate from this curve toward the curve for the strong confinement. It may be noted here that in the case of strong confinement it was assumed that the electrons and holes are not in the form of excitons as in the case of bulk ZnO or QZDs of larger sizes but rather they are in the unbound state though interacting strongly through Coulomb forces and localized in the QDs. Although one can find a number of models in the literature [62, 63, 65–67] to understand the bandgap versus size behavior of the dots, but we find that the classic model of the effective mass approximation as seen separately in strong and weak confinement regimes explained our experimental data rather satisfactorily.

Figure 3.24 shows the temperature-dependent PL spectra from the multilayer matrix of ZQDs of mean radius of about 2.3 nm in a broad range of 6–300 K. It can be seen that the PL spectra of ZQDs exhibit various spectral features which conspicuously broaden and shift toward red with increasing temperature. As can be seen in Fig. 3.24, the PL spectra were dominated by two sharp peaks at ~ 3.368 (SP) and ~ 3.360 eV (D^0P) in the temperature range of 6–50 K.

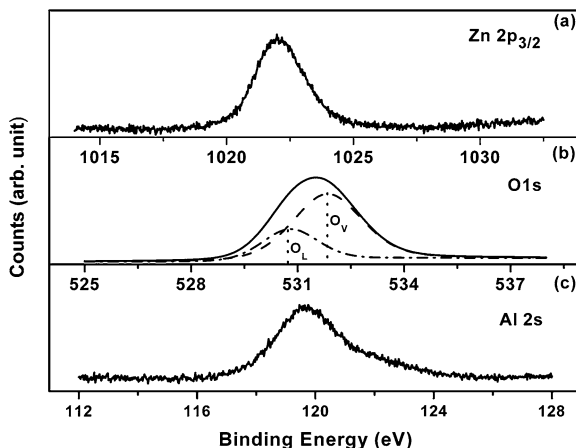
Adjacent to these peaks one can see a weak PL feature (A^0P) peaking at ~ 3.333 eV. Beyond these primary PL peaks there are prominent LO phonon replicas of SP and D^0P peaks seen at ~ 3.296 and 3.288 eV, respectively, and the corresponding 2LO phonon replicas at ~ 3.224 and 3.216 eV, respectively, which are which are ~ 72 and 144 meV away, respectively, from the parent PL peaks. Presence of LO and 2LO phonon replicas of the primary PL transitions is a noteworthy observation. As the sample temperature was increased, the primary PL peaks of SP, D^0P , and A^0P diminished, broadened, merged, and shifted to lower energies and at about 70 K a new feature appeared at ~ 3.376 eV. At temperatures beyond 70 K, this new feature started dominating over the merged feature of SP and D^0P as can be seen in Fig. 3.24.

In literature one can find number of reports on the PL spectroscopy of ZQDs but most of them are for ZQDs with mean size larger than the excitonic Bohr radius [68–70]. To the best of our knowledge, there is no detailed report on the

temperature-dependent PL characteristics of alumina capped ultra-small ZQDs grown by PLD whose mean size is smaller than the excitonic Bohr radius. Hence an assignment of various PL spectral features to understand their thermal dynamics shown in Fig. 3.24 of the present experiments is based on the existing literature on PL from the ZQDs grown mostly by wet chemical methods or bulk ZnO. It may also be noted here that the PL spectral features in case of ultra-small ZQDs are expected to be blue shifted compared to those in the larger ZQDs and that of the bulk ZnO but this blue shift might be mostly counterbalanced by the red shift due to the significant Stoke shift [59, 68] and/or the heating of the ZQDs by the laser beam used as excitation source. Hence the spectral positions of the PL features of the ultra-small ZQDs may not be very different from their larger counterparts. Another important point to be illustrated here is that the optical transitions in the ultra-small ZQDs are expected to be non-excitonic in nature while in case of ZQDs of larger sizes, the PL features are described and interpreted in terms of excitonic transitions. Hence in the present case of ultra-small QDs, the emanating PL has been considered as those due to the electron-hole pairs which are localized in the QDs and hence strongly interacting with each other but unbound. The PL peak SP at ~ 3.368 eV in the temperature range of 6–50 K could be attributed to the recombination due to surface O_V donor-bound electron-hole pairs [71, 72], while the peak D²P at ~ 3.360 eV could be due to the recombination of electron-hole pairs bound to the Al donors [73]. The presence of aluminum donors in the ZQDs is expected as Al₂O₃ has been used as capping as well as buffer layer in the ZQD multilayer structures. The PL peak A⁰P at ~ 3.333 eV in the literature has been attributed to the stacking faults bound electron-hole pair recombinations [73]. The PL feature at ~ 3.376 eV, which appeared at ~ 70 K and red shifted with increasing sample temperature could be assigned to the band-edge transition (BT) of the ZQDs' ensemble. The spectral position of the band-edge measured from the pertinent experimental photo-absorption spectrum shown in Fig. 3.23 for the ZQDs of mean radius 2.3 nm was at ~ 3.45 eV. It may be noted here that the energy difference between the location of BET at low temperature and the experimentally measured absorption band-edge at room temperature is about 166 meV, which has been attributed mainly to the Stoke shift of the BET in the ZQDs expected in the ultra-small ZQDs due to the large electrostatic attractive field between the confined electron and holes [68]. As also discussed above, the other possibility for this red shift of BET compared to absorption band-edge at room temperature could be the rise in local temperature of the ZQDs due to the absorption of the excitation light from the He–Cd laser. Alim et al. have shown that the local temperature of ZnO can significantly rise at this power level [38] which can correspondingly contribute to the red shift of the PL band-edge of the ZQDs' also.

To ascertain the origin of these spectral features, the chemical state of different elemental constituents of the ZQDs was studied using XPS. The XPS profiles of the 4 nm thick layer of ZnO originally sandwiched between the buffer and the capping layers of alumina is shown in Fig. 3.25. For this measurement, the capping layer of alumina was completely removed in situ by etching the sample

Fig. 3.25 X-ray photoelectron spectra of Zn 2p_{3/2} **a** O 1s and **b** and Al 2s **c** levels from 4 nm thick layer of ZnO originally sandwiched between buffer and capping layers of alumina. The capping layer was removed by in situ etching before recording these spectra. [Reprinted with permission from Kukreja et al. [59]. Copyright 2011 American Vacuum Society]

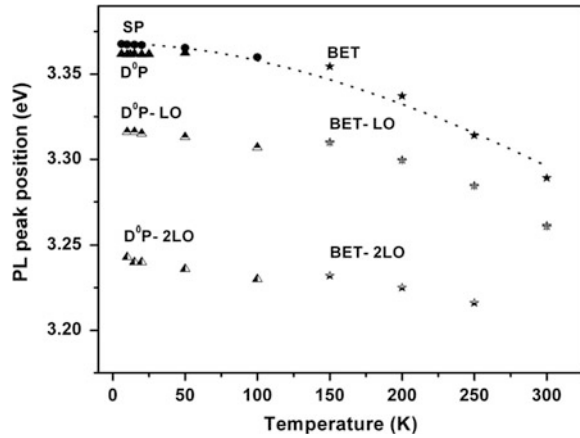


surface before measurements. The elemental presence of Zn, O, and Al in the ZnO layer can clearly be seen in Fig. 3.25 through the observed Zn 2p_{3/2}, O 1s, and Al 2s XPS peaks at binding energies ~ 1022 , 531.5, and 119.5 eV, respectively [74, 75]. Incorporation of Al in ZnO is possible due to interdiffusion and mixing of constituents at the interfaces of the buffer/capping layer and the ZnO layers during the PLD [25]. The spectrum corresponding to O 1s has been deconvoluted accurately when fitted with two peaks of Lorentzian mixed with Gaussian. The peak at ~ 530.15 eV designated as O_L has been attributed to O^{2-} ions on the lattice sites of hexagonal Zn^{2+} ion array and the peak at ~ 531.25 eV designated as (O_V) is associated with O^{2-} ions in the oxygen deficient regions within the matrix of ZnO [76]. As can be seen in Fig. 3.25, the peak corresponding to O_V which is the measure of the O^{2-} vacancies dominates over the peak corresponding to O_L . It has been reported in the literature that the oxygen vacancies which act as donors in ZnO are abundantly concentrated in the surface region [74, 76] and hence significant presence of donor-bound charge carriers in the surface region of the ZQDs is expected. In addition, the large surface to volume ratio of QDs supports the surface related recombination features further in the PL of ultra-small ZQDs.

The spectral positions of various PL peaks as a function of temperature are shown in Fig. 3.26. As can be seen at low temperatures, the PL recombinations are dominated by the SP peak and beyond ~ 125 K this peak merged with the higher energy feature corresponding to BET as mentioned earlier. The spectral position of the D⁰P transition as a function of temperature is shown in limited temperature range in which this transition was conspicuously observed. Spectral positions of the phonon replicas of SP and BET transitions are also shown in Fig. 3.26.

The variation of these spectral PL features can be fitted using the Varshni relation discussed in Eq. 3.16. The best fit with the experimental values, shown by the dotted curve in Fig. 3.26, was obtained with the fitting parameters $\alpha = 8.2 \times 10^{-4}$ eV/K and $\beta = 1070$ K. These values of fitting parameters matched well with those for bulk ZnO reported in the literature [68]. It can also be

Fig. 3.26 Spectral positions of different PL peaks from ZQDs as a function of temperature. The points are experimental values and the dotted curve is a theoretical fit based on Varshni's equation (Eq. 3.16). [Reprinted with permission from Kukreja et al. [59]. Copyright 2011 American Vacuum Society]

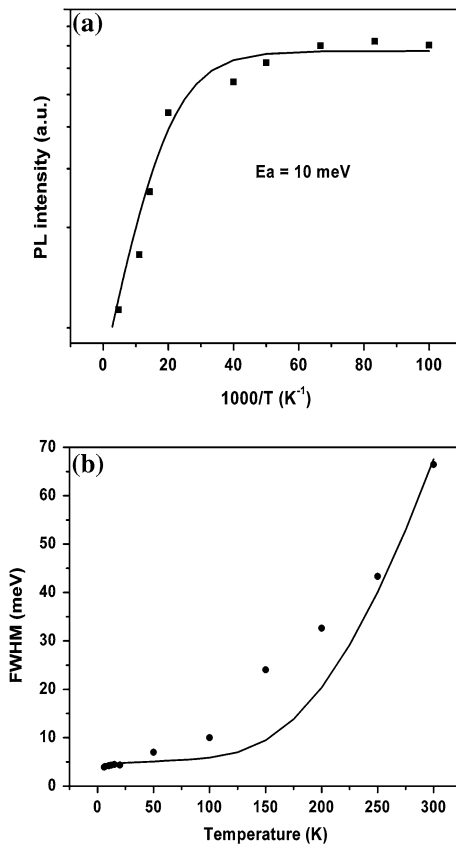


seen in Fig. 3.26 that the energy gap between the spectral positions of SP and BET PL peaks and that for their LO phonon replicas slightly decreased with the increase in the sample temperature. This can be attributed to the existence of bound exciton complexes in which the electron-hole pairs are bound to the surface defects and the transition shifts from one complex to another as the temperature increases. This possibility has been discussed in detail by Teke et al. for the single crystalline bulk ZnO [36].

The activation energy of SP transition at ~ 3.368 eV was estimated by plotting the integrated intensity of SP peak as a function of inverse temperature of the sample as shown in Fig. 3.27a. It can be clearly seen in this figure that the peak intensity follows the Arrhenius type of dependence on temperature given by the Eq. 3.15. The plot of the above equation is theoretical fit to data shown by the solid curve in Fig. 3.27a and from this fitting the activation energy E_a was found to be ~ 10 meV. This value of the activation energy corresponds to binding energy of electron-hole pairs with the donor type surface defects of the QDs and is comparable to the one reported in the literature [72].

The line width (FWHM) of the PL peaks as a function of temperature corresponding to the SP and BET recombinations is shown in Fig. 3.27b. The observed FWHM of these PL peaks is attributed to three broadening mechanisms which have been described by Hellmann and O'Neill formulation [46, 47] discussed in Eq. 3.19. In case of ZQDs, the Γ_{inh} is the inhomogeneous broadening due to the size variation of the ZQDs [60]. The second term in Eq. 3.19 is linear in temperature and is governed by the corresponding phonon scattering coefficient γ_{ph} and represents broadening due to scattering with acoustic phonons. The third term corresponds to the broadening due to scattering of charge carriers with LO phonons. In the original formulation of Hellmann and O'Neill [46, 47], they took excitons as recombining charge carriers and the third term actually corresponds to the coupling of LO phonons with excitons as per their formulation [46, 47]. However, since in the present case we think that optical transitions are non-excitonic in the ultra-small ZQDs, the coupling of LO phonons with the

Fig. 3.27 **a** Variation of peak intensity of the PL originating from the surface bound electron-hole pairs' recombination (SP) with inverse of temperature T . **b** Line width (FWHM) of the SP (up to 100 K) and band-edge transition BET (beyond 100 K) as a function of temperature. Discrete points are experimental values and continuous curves are theoretical fits. [Reprinted with permission from Kukreja et al. [59]. Copyright 2011 American Vacuum Society]



electron-hole pairs is expected to be different from that with the excitons as proposed by Hellmann and O'Neill in their formulations mainly due to the fact that excitons are bosons and unbound electrons and holes being Fermions will not follow the Bose statistics. To the best of our knowledge, the formulation of LO phonon coupling with the unbound electron-hole pairs does not exist in the literature. In the absence of any such model, we used the Hellmann and O'Neill model based on excitons. The best fit of the above equation with the FWHM shown in Fig. 3.27b was obtained for $\gamma_{ph} = 12 \mu\text{V/K}$ and $\Gamma_{LO} = 980 \text{ meV}$. Two points are worth noting here. First that the LO phonon coupling coefficient Γ_{LO} is significantly large and comparable to that of bulk ZnO [69]. The value of Γ_{LO} for isolated free standing ZQDs of $\sim 4 \text{ nm}$ diameter prepared by wet chemical method reported by Fonoberov is much lower than this [69]. Second, despite our best efforts to get a good fit, the calculated curve did not match very well with most of the experimental points in the intermediate range as can be seen in Fig. 3.27b. These observations lead to important conclusions for the ultra-small ZQDs. One is that the coupling of LO phonons with the recombining electron-hole pairs is significantly strong in the ultra-small ZQDs grown in the alumina host compared

to free standing ZQDs grown by wet chemical methods. This is contrary to the prevailing understanding that with decreasing size, the LO phonon coupling decreases [69, 71]. The strong coupling of the recombining electron-hole pairs with LO phonons is also clear from the presence of LO phonon replicas of SP and BET transitions seen in Fig. 3.24. This strong coupling of LO phonons with the recombining electron-hole pairs might be attributed to the quantum confinement effect, strain, and/or enhanced Coulombic interaction between the localized electrons and holes and the resulting Fröhlich interactions etc. In case of self-organized InAs/GaAs, Heitz et al. have shown that the interaction of LO phonon with excitons increased for such strained low-symmetry QDs because of the quantum confinement and piezoelectric effect [77]. Richters et al. have shown that coating of ZnO nanowire core with alumina shell strongly reduced the defects and enhanced the phonon interaction of the charged deep centers with the surrounding crystal lattice [78]. The other reason for this mismatch between the theoretical curve and the experimental points shown in Fig. 3.27b might be that the PL recombinations are non-excitonic in the present case. Since the theoretical formulation described by Hellmann and O'Neill is meant for the coupling of free excitons with LO phonons [46, 47], it may not match with the experimental points of the present experiment.

3.7 Conclusions

In conclusion, the temperature-dependent PL processes of the ZnO thin films grown on sapphire by PLD in the broad temperature range of 10–300 K gives insight into the various mechanisms and their relative influence on light emission, which in turn are related to the structural and crystalline quality of the films. In the present case since the dynamics of the PL processes was similar to that observed in bulk crystals of ZnO, it means reasonably good crystalline and structural quality of the PLD grown films on sapphire substrates. At low temperatures, the prominent PL peaks were due to neutral donor bound exciton and it is LO phonon-assisted transitions. With increasing temperatures, the free excitonic PL and associated phonon replicas dominated the PL spectra. The unusual temperature dependence of 1 and 2 LO phonon-assisted transitions of the F_X PL was explained by taking into account the kinetic energy of the gas like free excitons.

Photo luminescence spectroscopic investigation of ZnO MQWs of different well layer thicknesses grown on (0001) sapphire using an in-house developed buffer-assisted PLD scheme in the broad temperature range of 10 K to RT. Growth of ZnO/MgZnO MQWs was carried out on sapphire substrates using in-house developed buffer assisted PLD scheme. The 8 nm thick $Mg_{0.34}Zn_{0.66}O$ alloy films with bandgap of ~ 4.1 eV was used as barrier layer and ZnO well layer thickness was varied in the range from ~ 1 to 4 nm. Efficient room temperature PL was achieved on these MQWs which blue shifted with decreasing ZnO well layer thickness due to putative quantum confinement effects. The optical absorption

spectra of MQW structures showed monotonic blue shift in ZnO absorption edge and excitonic features entwined with the band-edges, which pointed to the excitonic nature of the PL transitions. At room temperature, the band-edge of these MQWs shifted from ~ 3.36 to 3.78 eV on decreasing the well layer thickness from ~ 4 to 1 nm in agreement with theoretically calculated values. In the range from 10 K to RT, the PL spectral line width increased and the peak shifted monotonically toward red with increasing temperature. The red shift of the PL peak with increasing temperature was attributed to the bandgap shrinkage in accordance with the Varshni's empirical relation. The increase in spectral line width with temperature was explained by considering the scattering of excitons with acoustic and optical phonons in different temperature regimes.

PL processes occurring in ensembles of alumina capped ZQDs grown using pulsed laser deposition were studied using temperature-dependent PL spectroscopy. The PL processes in alumina capped ultra-small ZQDs are different than those observed in their uncapped smaller or larger counterparts grown mostly by wet chemical routes. One basic difference is that the PL in alumina capped ultra-small ZQDs appears to be due to the localized electron-hole pairs instead of excitons. Therefore it is expected that the PL recombinations would be due to the electron-hole pairs and not through the excitonic recombinations. At low temperatures the PL spectra were dominated by the surface bound electron-hole pairs' recombinations mainly because of large surface to volume ratio and presence of oxygen vacancies in the surface region of the ultra-small ZQDs. The Al donor bound electron-hole pair recombinations are also observed because of the sputtering based mixing at the interfaces during the PLD and the diffusion of Al from the capping and/or buffer layers of alumina into the ZQDs. The band-edge PL transitions, red shifted by ~ 166 meV with respect to the experimentally observed absorption band-edge due to Stokes shift and/or local heating of the ZQDs was observed only when the sample temperature was 70 K and higher. A small PL peak due to the defect bound recombination at ~ 3.333 eV was also observed. The LO phonon coupling with the electron-hole pairs responsible for the PL emission is significantly large in the alumina capped ultra-small ZQDs. This is also evident from the presence of LO and 2LO phonon replicas in the PL spectra and the FWHM of the PL peak as a function of temperature. This is in contrast to the popular thought that LO phonon coupling with excitons decreases with decreasing size of the ZQDs.

Acknowledgments It is a pleasure to thank Prof. C. Klingshirn of University of Karlsruhe, Germany, Dr. G. M. Prinz and Dr. K. Thonke of Institut für Halbleiterphysik, Universität Ulm, Germany, and Dr. T. K. Sharma, Mr. Sanjay Porwal, and Dr. S. M. Oak of Raja Ramanna Centre for Advanced Technology, Indore for their help with the PL measurements and many fruitful discussions. We also thank Dr. T. Ganguli, Dr. A. K. Shrivastava, and Dr. S. K. Deb of our centre for their help with HRXRD and TEM measurements and Dr. D. M. Phase and Mr. A. Wadikar of UGC—DAE Centre for Scientific Research, Indore for their help with the XPS measurements. LMK thanks Alexander von Humboldt foundation of Germany for the financial support to visit University of Karlsruhe and Universität Ulm where low temperature PL studies were carried out.

References

1. Ü. Özgür, Ya.I. Alivov, C. Liu, A. Teke, M. A. Reshchikov, S. Doğan, V. Avrutin, S.-J. Cho, H. Morkoç, *J. Appl. Phys.* **98**, 041301 (2005)
2. C. Klingshirn, *Chem. Phys. Chem.* **8**, 782 (2007)
3. A. Tsukazaki, A. Ohtomo, T. Onuma, M. Ohtani, T. Makino, M. Sumiya, K. Ohtani, S.F. Chichibu, S. Fuke, Y. Segawa, H. Ohno, H. Koinuma, M. Kawasaki, *Nat. Mater.* **4**, 42 (2005)
4. Y.R. Ryu, T.S. Lee, J.A. Lubguban, H.W. White, Y.S. Park, C.J. Youn, *Appl. Phys. Lett.* **87**, 153, 504 (2005)
5. W.I. Park, J.S. Kim, G.-C. Yi, H.-J. Lee, *Adv. Mater.* **17**, 1393 (2005)
6. P. Misra, A.K. Das, L.M. Kukreja, *Phys. Status Solidi C* **7**(6), 1718 (2010)
7. P. Sharma, A. Mansingh, K. Sreenivas, *Appl. Phys. Lett.* **80**, 553 (2002)
8. A. Mang, K. Reimann, St. Rubenacke, *Solid State Commun.* **94**, 251 (1995)
9. A.Y. Polyakov, N.B. Smirnov, A.V. Govorkov, E.A. Kozhukhova, V.I. Vdovin, K. Ip, M.E. Overberg, Y.W. Heo, D.P. Norton, S.J. Pearton, J.M. Zavada, *J. Appl. Phys.* **94**, 2895 (2003)
10. S.O. Kucheyev, J.S. Williams, C. Jagadish, J. Zou, C. Evans, A.J. Nelson, A.V. Hamza, *Phys. Rev. B* **67**, 094115 (2003)
11. V.A. Coleman, C. Jagadish, *Basic Properties and Applications of ZnO*, in *Zinc Oxide Bulk, Thin Films and Nanostructures: Processing, Properties, and Applications*, ed. by C. Jagadish, S.J. Pearton (Elsevier, 2006)
12. R. Triboulet, J. Perriere, *Prog. Cryst. Growth Charact. Mater.* **47**, 65 (2003)
13. T. Fukumura, H. Toyosaki, Y. Yamada, *Semicond. Sci. Technol.* **20**, S103–S111 (2005)
14. D.M. Bagnall, Y.F. Chen, Z. Zhu, T. Yao, S. Koyama, M.Y. Shen, T. Goto, *Appl. Phys. Lett.* **70**, 2230 (1997)
15. A. Ohtomo, K. Tamura, M. Kawasaki, T. Makino, Y. Segawa, Z.K. Tang, G.K.L. Wong, Y. Matsumoto, H. Koinuma, *Appl. Phys. Lett.* **77**, 2204 (2000)
16. H.D. Sun, T. Makino, N.T. Tuan, Y. Segawa, Z.K. Tang, G.K.L. Wong, M. Kawasaki, A. Ohtomo, K. Tamura, H. Koinuma, *Appl. Phys. Lett.* **77**, 4250 (2000)
17. T. Ohnishi, A. Ohtomo, M. Kawasaki, K. Takahashi, Y. Yoshimoto, *Appl. Phys. Lett.* **72**, 824 (1998)
18. J.I. Pankove, *Optical Processes in Semiconductors* (Dover Publications, New York, 1971)
19. L. Birman, *Phys. Rev. Lett.* **2**, 157 (1959)
20. *Landolt-Börnstein*, New Series, Group III, vol. 17 B, 22, 41B, ed. by U. Rössler, (Springer, Heidelberg, 1999)
21. C. Klingshirn, *Semiconductor Optics*, 3rd edn. (Springer, Heidelberg, 2006)
22. J.H. Davies, *The Physics of Low-Dimensional Semiconductors* (Cambridge University Press, Cambridge, 1998)
23. P. Harrison, *Quantum Wells* (Wires and Dots, New York, 2000)
24. P.K. Basu, *Theory of Optical Processes in Semiconductors: Bulk and Microstructures* (Clarendon Press, Oxford, 1997)
25. L.M. Kukreja, B.N. Singh, P. Misra, *Pulsed Laser Deposition of Nanostructured Semiconductors*, in *Bottom-up Nanofabrication: Supramolecules, Self-Assemblies and Organized Films*, ed. by K. Ariga, H.S. Nalwa, (American Scientific, California, 2008)
26. P. Misra, L.M. Kukreja, *Thin Solid Films* **485**(1–2), 42 (2005)
27. P. Misra, T.K. Sharma, L.M. Kukreja, *Curr. Appl. Phys.* **9**(1), 179 (2009)
28. A. Ohtomo, M. Kawasaki, T. Koida, K. Masubuchi, H. Koinuma, Y. Sakura, Y. Yashida, T. Yashuda, Y. Segawa, *Appl. Phys. Lett.* **72**, 2466 (1998)
29. C. Klingshirn, *Phys. Status Solidi B* **71**, 547 (1975)
30. D.C. Reynolds, D.C. Look, B. Jogai, C.W. Litton, T.C. Collins, W. Harsch, G. Cantwell, *Phys. Rev. B* **57**, 12151 (1998)
31. D.W. Hamby, D.A. Lucca, M.J. Klopstein, G. Cantwell, *J. Appl. Phys.* **93**, 3214 (2003)

32. C. Solbrig, E. Mollwo, *Solid State Commun.* **5**, 625 (1975)
33. Y. Chen, D.M. Bagnall, H.-J. Koh, K.-T. Park, K. Hiraga, Z. Zhu, T. Yao, *J. Appl. Phys.* **84**, 3912 (1998)
34. D.M. Bagnall, Y.F. Chen, M.Y. Shen, Z. Zhu, T. Goto, T. Yao, *J. Cryst. Growth* **184/185**, 605 (1998)
35. S. Bethke, H. Pan, B.W. Wessels, *Appl. Phys. Lett.* **52**, 138 (1998)
36. A. Teke, Ü. Özgür, S. Doğan, X. Gu, H. Morkoç, B. Nemeth, J. Nause, H.O. Everitt, *Phys. Rev. B* **70**, 195207 (2004)
37. Douglas B. Chrisey, Graham K. Hubler, *Pulsed Laser Deposition of Thin Films*, (Wiley-interscience, 1994)
38. A. Alim Khan, A. Fonoberov Vladimir, A. Balandin Alexander, *Appl. Phys. Lett.* **86**, 053103 (2005)
39. M.S. Liu, L.A. Bursill, S. Praver, K.W. Nugent, Y.Z. Tong, G.Y. Zhang, *Appl. Phys. Lett.* **74**, 3125 (1999)
40. E. Gross, S. Permogorov, B. Razbirin, *J. Phys. Chem. Solids* **27**, 1647 (1966)
41. T. Makino, Y. Segawa, M. Kawasaki, H. Koinuma, *Semicond. Sci. Technol.* **20**, 78 (2005)
42. M.H. Huang, S. Mao, H. Feick, H. Yan, Y. Wu, H. Kind, A. Dadgar, E. Weber, R. Russo, P. Yang, Room-temperature ultraviolet nanowire nanolasers. *Science* **292**, 1897 (2001)
43. P. Misra, T.K. Sharma, S. Porwal, L.M. Kukreja, *Appl. Phys. Lett.* **89**, 161912 (2006)
44. A. Ohtomo, A. Tsukazaki, *Semicond. Sci. Technol.* **20**, 1 (2005)
45. P. Misra, T.K. Sharma, G.M. Prinz, K. Thonke, L.M. Kukreja, in *Proceedings IUMRS-ICAM, Bangalore, Oct 7–12 2007*, pp. V11–12
46. R. Hellmann, M. Koch, J. Feldmann, S.T. Condiff, E.O. Gobel, D.R. Yakovlev, A. Waag, G. Landwehr, *Phys. Rev. B* **48**, 2847 (1993)
47. M. O'Neill, M. Oestreich, W.W. Ruhle, D.E. Ashenford, *Phys. Rev.* **48**, 8980 (1993)
48. Y.P. Varshni, *Physica* **34**, 149 (1967)
49. B.P. Zhang, N.T. Binh, K. Wakatsuki, C.Y. Liu, Y. Segawa, N. Usami, *Appl. Phys. Lett.* **86**, 032105 (2005)
50. T. Mozume, J. Kasai, *J. Appl. Phys.* **95**, 1050 (2004)
51. P. Misra, T.K. Sharma, L.M. Kukreja, *Superlattices Microstruct.* **42**(1–6), 212–217 (2007)
52. U. Koch, A. Fojtik, H. Weller, A. Henglein, *Chem. Phys. Lett.* **122**, 507 (1985)
53. L. Spanhel, M.A. Anderson, *J. Am. Chem. Soc.* **113**, 2826 (1991)
54. E.M. Wong, J.E. Bonevich, P.C. Searson, *J. Phys. Chem. B* **102**, 7770 (1998)
55. J.J. Cavaleri, D.E. Skinner, D.P. Colombo Jr, R.M. Bowman, *J. Chem. Phys.* **103**, 5378 (1995)
56. E.M. Wong, P.C. Searson, *Appl. Phys. Lett.* **74**, 2939 (1999)
57. I. Ohkubo, Y. Matsumoto, A. Ohtomo, T. Ohnishi, A. Tsukazaki, M. Lippmaa, H. Koinuma, M. Kawasaki, *Appl. Surf. Sci.* **159–160**, 514 (2000)
58. S. Barik, A.K. Srivastava, P. Misra, R.V. Nandedkar, L.M. Kukreja, *Solid State Commun.* **127**, 463 (2003)
59. L.M. Kukreja, P. Misra, A.K. Das, J. Sartor, H. Kalt, *J. Vac. Sci. Technol., A* **29**(3), 120 (2011)
60. L.M. Kukreja, S. Barik, P. Misra Jr, *Cryst. Growth* **268**(3–4), 531 (2004)
61. L.M. Kukreja, P. Misra, J. Fallert, J. Sartor, H. Kalt, C. Klingshirn, *IEEE Photon. Global* **1** (2009)
62. L.E. Brus, *J. Chem. Phys.* **80**, 4403 (1984)
63. Y. Kayanuma, *Phys. Rev. B* **38**, 9797 (1988)
64. Y. Kayanuma, *Phys. Rev. B* **38**, 9797 (1988)
65. M.V. Rama Krishna, R.A. Friesner, *Phys. Rev. Lett.* **67**, 629 (1991)
66. P.E. Lippens, M. Lannoo, *Phys. Rev. B* **39**, 10935 (1989)
67. S.V. Nair, L.M. Ramaniah, K.C. Rustagi, *Phys. Rev. B* **45**, 5969 (1992)
68. K.-F. Lin, H.-M. Cheng, H.-C. Hsu, L.-J. Lin, W.-F. Hsieh, *Chem. Phys. Lett.* **409**, 208 (2005) and references cited therein
69. V.A. Fonoberov, K.A. Alim, A.A. Balandin, F. Xiu, J. Liu, *Phys. Rev. B* **73**, 165317 (2006)

70. W.-T. Hsu, K.-F. Lin, W.-F. Hseih, *Appl. Phys. Lett.* **91**, 181913 (2007)
71. V.V. Travnikov, A. Freiberg, S.F. Savikhin, *J. Lumin.* **47**, 107 (1990)
72. L. Wischmeier, T. Voss, I. Ruckmann, J. Gutowski, *Nanotechnology* **19**, 135705 (2008)
73. B.K. Meyer et al., *Phys. Status Solidi B* **241**, 231 (2003)
74. M. Chen, X. Wang, Y.H. Yu, Z.L. Pei, X.D. Bai, C. Sun, R.F. Huang, L.S. Wen, *Appl. Surf. Sci.* **158**, 134 (2000)
75. N. Ohtsu, M. Oku, T. Shishido, K. Wagatsuma, *Appl. Surf. Sci.* **253**, 8713 (2007)
76. M.N. Islam, T.B. Ghosh, K.L. Chopra, H.N. Acharya, *Thin Solid Films* **280**, 20 (1996)
77. R. Heitz, I. Mukhametzhanov, O. Stier, A. Madhukar, D. Bimberg, *Phys. Rev. Lett.* **83**, 4654 (1999)
78. J.-P. Richters, T. Voss, D.S. Kim, R. Scholz, M. Zacharias, *Nanotechnology* **19**, 305202 (2008)